Eurographics Symposium on Geometry Processing 2025
M. Attene and S. Sellán
(Guest Editors)

Volume 44 (2025), Number 5

An Efficient Global-to-Local Rotation Optimization Approach via Spherical Harmonics

Zihang He[†1] Yuezhi Yang[2] Congyue Deng[2‡] Jiaxin Lu[1] Leonidas Guibas[2] Qixing Huang[1§]

[1]The University of Texas at Austin [2]Stanford University

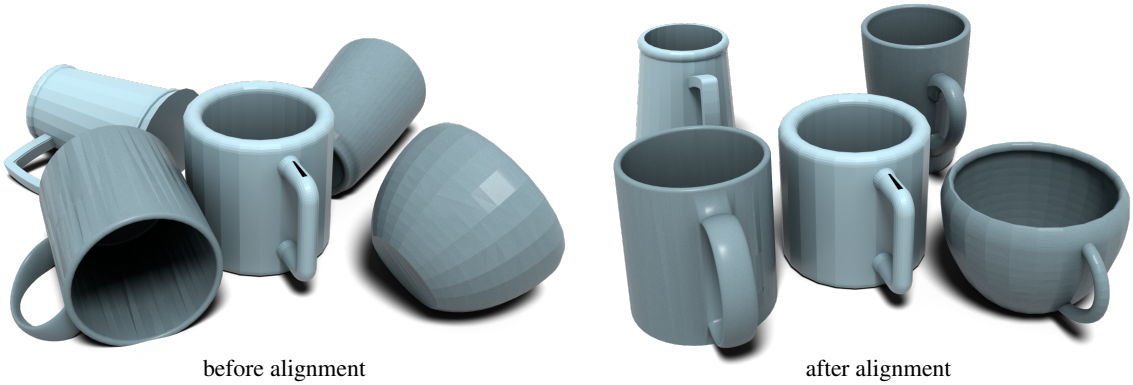

before alignment after alignment

Figure 1: *Our method computes the relative rotation between two normalized shapes by aligning spherical harmonic coeffecients*

Abstract

This paper studies the classical problem of 3D shape alignment, namely computing the relative rotation between two shapes (centered at the origin and normalized by scale) by aligning spherical harmonic coefficients of their spherical function representations. Unlike most prior work, which focuses on the regime in which the inputs have approximately the same shape, we focus on the more general and challenging setting in which the shapes may differ. Central to our approach is a stability analysis of spherical harmonic coefficients, which sheds light on how to align them for robust rotation estimation. We observe that due to symmetries, certain spherical harmonic coefficients may vanish. As a result, using a robust norm for alignment that automatically discards such coefficients offers more accurate rotation estimates than the widely used L2 norm. To enable efficient continuous optimization, we show how to analytically compute the Jacobian of spherical harmonic coefficients with respect to rotations. We also introduce an efficient approach for rotation initialization that requires only a sparse set of rotation samples. Experimental results show that our approach achieves better accuracy and efficiency compared to baseline approaches.

CCS Concepts

• ***Computing methodologies*** → ***Shape analysis; Volumetric models;***

1. Introduction

Estimating the relative pose between two 3D shapes is a fundamental problem in many applications. A relative pose consists of a scaling component, a translation component, and a rotation component. The scaling and translation components can be computed using standard normalization procedures, e.g., the barycenter of each shape is at the origin, and the trace norm of each shape moment is 1. In contrast, normalizing the rotation component (e.g., using principal directions of the second-order shape moment) is extremely difficult. It turns out that the most reliable approach is to optimize a matching loss in the rotation space $\mathrm{SO}(3)$, cf. [Kaz07]. This problem is quite challenging, as the optimization problem is usually non-convex and has many local minima.

To this end, remarkable progress has been achieved by converting 3D shapes into spherical functions and aligning coefficients of spherical harmonics (i.e., Fourier bases on spheres) for relative rotation estimation [MPD06, MD06, FRB08, HSZ*05, Kaz07]. In particular, under the Euler angle representation, the Wigner-D matrix [HMR09] allows us to compute the L^2 distance between the coefficients of

† zhhe@utexas.edu
‡ congyue@stanford.edu
§ huangqx@utexas.edu

spherical harmonics with time complexity $O(b^4)$ on a grid of resolution b^3, where b is the number of samples in each Euler angle. However, for real-time performance, even with this fast algorithm, we can only use a small b ($b \leq 40$), leading to an angular error from 10° to 20°. This error is significant for many downstream applications. Although there are more efficient approaches, e.g., [Kaz07], these are typically approximate and there are performance gaps from the original formulation. In addition to efficiency, another issue is that the L^2 norm does not offer good performance between two shapes with large shape variations (see Figure 1).

In addition to aligning 3D shapes, developing a principled approach for rotation alignment of spherical harmonics has far-reaching implications in many other areas. One example is to construct equivariant/invariant neural networks using spherical harmonics. An accurate and efficient relative rotation estimation approach allows us to align spherical harmonics in a shared coordinate system for representation learning, in which representations and rotations are jointly optimized. Otherwise, we have to use the expensive Wigner-D matrix representation [TSK*18, PRPO19, EAMD20, PG21] to model invariance/equivariance, introducing redundancies across different layers.

In this paper, we study the problem of relative rotation estimation using spherical harmonics from the lens of numerical optimization. We present three key contributions. First, we develop a simple, analytical, and sparse expression of the derivatives of spherical harmonic coefficients with respect to rotations. We show that this Jacobian allows efficient continuous optimizations, e.g., using the Gauss-Newton method.

Second, we present a stability analysis of the spherical harmonic coefficients under perturbed spherical functions. One key insight is that some coefficients vanish and aligning these coefficients is essentially aligning noise, which does not offer useful constraints. Therefore, when two input shapes are less similar, using a robust norm to align spherical harmonic coefficients can automatically discard the alignments of those vanishing coefficients, leading to improved alignment results.

Third, we introduce an approach to compute a candidate set of initial rotations for local refinement. Our approach only requires computing the alignment scores using a low-resolution Wigner-D matrix. We show how to extract potential local minima from a sparse set of samples, using both the alignment scores and the derivatives of the alignment scores computed from the Jacobian described above. Together, these three contributions lead to an efficient and robust relative rotation estimation pipeline.

We have evaluated our approach on the ShapeNetPart dataset [YKC*16]. Experimental results show that our approach outperforms baseline approaches both quantitatively and qualitatively. An ablation study justifies the effectiveness of the three key contributions of our approach, i.e., a local optimization procedure that uses the Gauss-Newton method, a robust norm to align spherical harmonic coefficients, and an efficient approach to detect candidate local minima.

2. Related Work

2.1. Rotation Estimation

Early approaches in rotation estimation are based on principal component analysis (PCA) and aligning principal directions with the axes. As pointed out in the seminar paper [KFR03], this approach does not work well when the principal values are close to each other. In addition, it is difficult to determine orientations such as up-and-down and left-and-right. Additional efforts are needed to address such ambiguities, cf. [RL18].

Another approach to relative rotation estimation or relative rigid pose estimation is to detect and match features that satisfy the rigidity constraints. These include RANSAC [SWK07], general Hough transform [MGP06, PMW*08, MAM14], and their variants [AMC08, BTP13]. We refer to [TCL*13] for a survey on this topic. These approaches are designed to match different scans of the same object. Their advantages are in matching partially overlapped and incomplete scans. However, they do not apply well when two objects have different geometric shapes, where it is very difficult to compute invariant feature points and feature descriptors.

A more robust way is to optimize a matching function in the space of $\mathrm{SO}(3)$. Usually, the function is non-convex, requiring an initial solution to begin with. This requires efficient methods to sample $\mathrm{SO}(3)$, and many methods [Kar07, Mar72, Mit08, YJLM10, Ale22] have been introduced in the literature. However, these methods have focused on generating samples that are evenly distributed in $\mathrm{SO}(3)$. Although they can be applied to any matching function, they are inefficient as evaluations at different samples are independent. This issue is partially addressed using spherical harmonics to define the matching function, which we will discuss in Section 2.3.

Learning-based approaches have also been introduced for relative rotation estimation. A common paradigm [KGC15, CHSA21] is to extract features from input objects, which are fed into a correlation module for the estimation of poses. Several methods have shown impressive results in the setting of matching 3D scans of an object or a 3D scene, including DCP [LWZ*19], PNetLK [AGSL19], FCGF [CPK19], Predator [HGU*21], RoReg [WLH*23], and GeoTF [QYW*23]. Although it is possible to extend these approaches to estimate the relative rotation between similar but different objects, a fundamental issue of learning-based approaches is the generalization issue and the challenge in handling uncertainties in the output, e.g., due to symmetries. Another issue is the need to have a larger perturbed dataset, larger networks, which results in larger learning and processing time.

2.2. Spherical Harmonics

Spherical harmonics form a frequency-space basis for representing functions defined over the sphere. They are the spherical analogue of the 1D Fourier series. Spherical harmonics have been used in a wide range of scientific domains [MS67, Tin03]. Spherical harmonics also have direct applicability in rendering [CMS87, SAWG91, Ram02, Gre03, Wym04, Slo08]. An important property of spherical harmonics is that a rotated spherical basis can be expressed as the linear combination of spherical bases of the same frequency, cf. [Gre03]. In addition, the L^2 norm of the coefficients of the same frequency remains constant under rotation. In the literature, people have explored

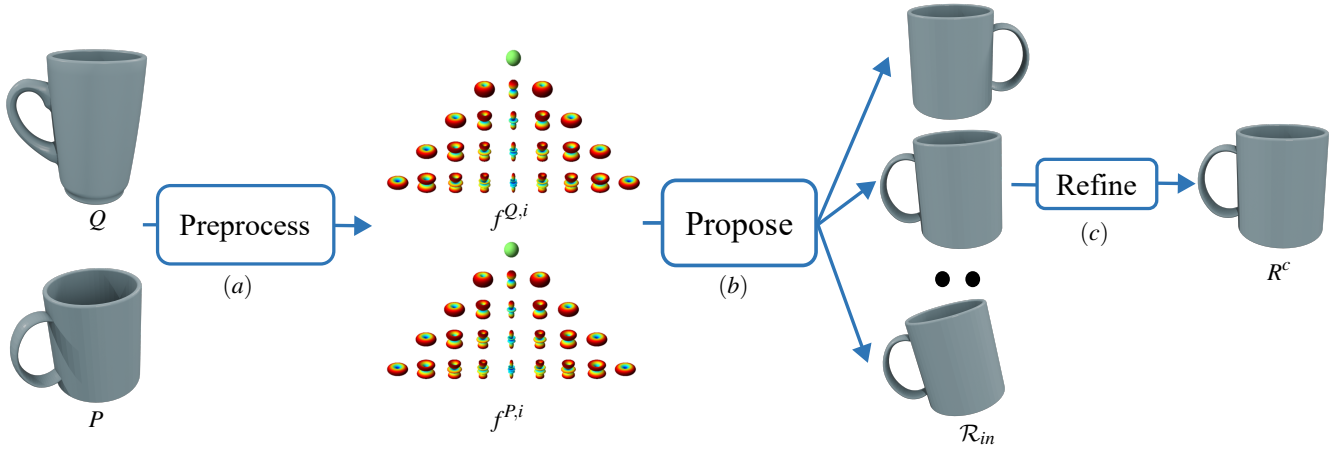

Figure 2: *Our approach has three stages. (a) The first stage converts the input shapes into a series of paired spherical functions. (b) The second stage predicts a candidate set of relative rotations using a weighted L2-norm between SH coefficients evaluated on a sparse set of rotation samples. (c) The third stage performs robust local refinement from each candidate rotation and returns the global minimum.*

these properties to develop rotation-invariant shape descriptors for shape retrieval purposes [KFR03]. [MZA*18] introduced invariant descriptors based on radial Hahn moments, which extend spherical harmonics. In contrast, this paper studies how to align the spherical harmonic coefficients for relative rotation estimation.

Symmetry detection using spherical harmonics has been studied in [KCD*04, Rus07, KKP13, LJYL16]. In the seminal paper [MSHS06], the authors introduced an approach to derive global rotational symmetries using polynomial moments that can be computed efficiently using spherical harmonics. The stability analysis results in this paper are based on the foundation work in [AB63], which is systematically introduced in [BC10]. In this paper, we focus on how to use these results to develop a robust objective function for the estimation of relative rotation.

2.3. Rotation Estimation Using Spherical Harmonics

A fundamental challenge of using spherical harmonic coefficients for rotation estimation is that the coefficients are polynomials of the rotation matrix, in which the order of the polynomial is the frequency order of the associated basis function. This makes it difficult to derive closed-form solutions that align spherical harmonics, cf. [HTB18]. In fact, the most efficient algorithms for computing these polynomials are based on recursion [IR98, CIGR99].

An important development in spherical harmonics is that, under the Euler angle representation, the coefficients under a rotation are decoupled into transformations under different Euler angles [BH95, RK99]. This leads to an algorithm (similar to the fast Fourier transform) that computes the correlations between the rotated coefficients of one function and the coefficients of another function under a uniform sampling of Euclidean angles [MPD06, MD06, FRB08, HSZ*05]. This algorithm, which involves the representation of the Wigner-D matrix [HMR09], has stimulated a wave of development of equivariant / invariant 3D neural networks [TSK*18, PRPO19, EAMD20, PG21].

However, this algorithm is still expensive, prohibiting one from obtaining accurate solutions that require a very dense sampling grid. [Kaz07] introduced an approach that first predicts the rotation axis, followed by a prediction of the rotation angle. Yet, this approach comes with an approximation, and there is a gap between the more expensive but accurate approach.

Our approach advances this line of work by introducing a novel objective function for rotation optimization and a local optimization approach that can refine an initial rotation. This local optimization approach is extremely fast, allowing us to test multiple initial rotations. Compared to prior work [SKS09, SFM09] that performs alternating optimization of Euler angles, our approach enables Gauss-Newton optimization of rotations and is much faster. The efficiency of our approach enables us to apply the Wigner-D matrix on a coarse grid and extract a candidate set of initial rotations for refinement.

3. Overview

The input of our approach consists of a source shape P and a target shape Q. We assume that they are normalized so that for each shape $x \in \{P, Q\}$

$$c_x = 0, \quad \operatorname{tr}(C_x) = 1.$$

where $c_x \in \mathbb{R}^3$ and $C_x \in \mathbb{R}^{3\times 3}$ are the barycenter and the moment matrix of x, which are computed from uniform point samples on x.

As shown in Figure 2, the key idea of our approach is to preprocess each input shape into a sequence of spherical functions, i.e., $f^{P,i}, 1 \le i \le n_r$ for P and $f^{Q,i}, 1 \le i \le n_r$ for Q, which are signed distance functions of P and Q on spheres with increasing radii. We will encode these spherical functions using spherical harmonic coefficients. With $f_l^{P,i}(R) \in \mathbb{R}^{2l+1}, 1 \le l \le l_{\max}$ and $f_l^{Q,i}(R) \in \mathbb{R}^{2l+1}, 1 \le l \le l_{\max}$ we denote coefficient vectors of l-th order of $f^{P,i}$ and $f^{Q,i}$ under rotation R in their own coordinate system. The definitions of spherical harmonics and their properties are introduced in Section 4. The construction of $f^{P,i}$ and $f^{Q,i}$ will be described in Section 7.1.

We formulate relative optimization as finding the global optimum

of the following optimization problem:

$$\operatorname*{argmin}_R e(R), \qquad e(R) = \sum_{i=1}^{n_r} \sum_{l=1}^{l_{\max}} w_{il} \|f_l^{P,i}(R) - f_l^{Q,i}\|^2. \tag{1}$$

Note that, unlike prior work [HSZ*05, SFM09] that uses uniform weights $w_{il} = 1$, our analysis in Section 6 shows that it is important to use weights that are tailored for different frequencies. In Section 7.2 and Section 7.3, we will introduce a global-2-local optimization strategy to solve Eq. (1).

In the following, we will first review the basics of spherical harmonics in Section 4. We then introduce two technical contributions of this paper, that is, the Jacobian of rotating spherical harmonics (Section 5) and the stability of spherical harmonic coefficients (Section 6).

4. Technical Background

This section introduces relevant technical background material of spherical harmonics, which we will use in this paper.

4.1. Spherical Harmonics

A function f on a sphere is typically expressed using the spherical coordinates (θ, ϕ) or the corresponding Cartesian coordinates $(x, y, z) = (\sin\theta\cos\phi, \sin\theta\sin\phi, \cos\theta)$. The norm of a function f and the inner product between two functions f and g are given by

$$\|f\|^2 = \int_{\theta=0}^{\pi} \int_{\phi=0}^{2\pi} f^2(\theta,\phi) sin\theta d\phi d\theta,$$
$$\langle f, g\rangle = \int_{\theta=0}^{\pi} \int_{\phi=0}^{2\pi} f(\theta,\phi) g(\theta,\phi) sin\theta d\phi d\theta.$$

The Fourier bases for spherical functions are the so-called spherical harmonics

$$Y_l^m(\theta,\phi) = \begin{cases} \sqrt{2} K_l^m \cos(m\phi) P_l^m(\cos\theta) & m > 0 \\ K_l^0 P_l^0(\cos(\theta)) & m = 0 \\ \sqrt{2} K_l^m \sin(-m\phi) P_l^{-m}(\cos\theta) & m < 0 \end{cases} \tag{2}$$

where K_l^m and the associated Legendre polynomials $P_l^m(z)$ are given by

$$K_l^m = \sqrt{\frac{2l+1}{4\pi} \frac{(l-|m|)!}{(l+|m|)!}}, \quad P_l^m(z) = \frac{(-1)^m}{2^l l!} (1-z^2)^{\frac{m}{2}} \frac{\partial^{l+m}(x^2-1)^l}{\partial^{l+m} x}.$$

$P_l^m(z)$ can be efficiently computed using recursion [PTVF92].

$Y_l^m(\theta,\phi)$ form an orthonormal basis for spherical functions. Specifically, for any function $f(\theta,\phi)$, in which $\|f\|^2 < \infty$, we have

$$f(\theta,\phi) = \sum_{l=0}^{\infty} \sum_{m=-l}^{l} f_l^m Y_l^m(\theta,\phi), \qquad f_l^m = \langle f, Y_l^m\rangle. \tag{3}$$

The sum $\sum_{l=0}^{l_{\max}} \sum_{m=-l}^{l} f_l^m Y_l^m(\theta,\phi)$ offers an approximation of f that preserves its low-frequency components up to $l_{\max}$. Aligning the coefficients f_l^m and g_l^m for a reasonable $l_{\max}$ becomes a natural objective to estimate the underlying rotation between f and g. To this end, we need to understand how to describe rotated spherical functions using spherical harmonics, which we will describe next.

4.2. Rotating Spherical Harmonics and the Wigner-D Matrix

Denote the Cartesian coordinates as $p = (x, y, z)^T$. We define the rotated function of f under R as

$$f_R(p) = f(R^T p).$$

f_R is also a spherical function. Consider its Fourier series:

$$f_R(\theta,\phi) = \sum_{l=0}^{\infty} \sum_{m=-l}^{l} f_l^m(R) Y_l^m(\theta,\phi),$$

where $f_l^m(I_3) = f_l^m$. A very important property regarding spherical harmonics is that $f_l^m(R)$ is a weighted combination of $f_l^{m'}, -l \le m' \le l$ where the weight of each $f_l^{m'}$ is a function of R. Moreover,

$$\sum_{m=-l}^{l} f_l^m(R)^2 = \sum_{m=-l}^{l} f_l^{m2}.$$

On the other hand, each weight is a polynomial of R of order l. For an arbitrary rotation R, the most effective way to compute $f_l^m(R)$ is through recursion [IR98].

Analytically, the simplest expression $f_l^m(R)$ comes from the Euler angle (α,β,γ) expression of a rotation $R(\alpha,\beta,\gamma) =$

$$\begin{pmatrix} \cos\alpha & -\sin\alpha & 0 \\ \sin\alpha & \cos\alpha & 0 \\ 0 & 0 & 1 \end{pmatrix} \begin{pmatrix} \cos\beta & 0 & -\sin\beta \\ 0 & 1 & 0 \\ \sin\beta & 0 & \cos\beta \end{pmatrix} \begin{pmatrix} \cos\gamma & -\sin\gamma & 0 \\ \sin\gamma & \cos\gamma & 0 \\ 0 & 0 & 1 \end{pmatrix}. \tag{4}$$

Under Eq. (4), $f_l^m(R)$ admits the following expression using the Wigner-D representation $D_{mn}^l(\alpha,\beta,\gamma)$, cf. [SFM09, BH95, RK99],

$$f_l^m(\alpha,\beta,\gamma) = \sum_{n=-l}^{l} D_{mn}^l(\alpha,\beta,\gamma) f_l^n \tag{5}$$

where

$$D_{mn}^l(\alpha,\beta,\gamma) = \mathrm{Re}\big(e^{-i\gamma m} d_{mn}^l(\beta) e^{-i\alpha m}\big) \tag{6}$$

and

$$d_{mn}^l(\beta) = \sum_{t=\max(0,n-m)}^{\min(l+n,l-m)} (-1)^t \frac{\sqrt{(l+n)!(l-n)!(l+m)!(l-m)!}}{(l+n-t)!(l-m-t)!(t+m-n)!t!} \Big(\frac{\cos(\beta)}{2}\Big)^{2l+n-m-2t} \Big(\frac{\sin(\beta)}{2}\Big)^{2l+m-n}.$$

Let

$$\xi = \alpha - \pi/2, \qquad \eta = \pi - \beta, \qquad \omega = \gamma - \pi/2.$$

We can rewrite

$$\begin{aligned} D_{mn}^l(\alpha,\beta,\gamma) &= \sum_h D_{mh}^l(\xi,\pi/2,0) D_{hn}^l(\eta,\pi/2,\omega) \\ &= \sum_h d_{mh}^l d_{hn}^l \exp\big(-i(m\xi + h\eta + n\omega)\big) \end{aligned} \tag{7}$$

where $d_{mn}^l = d_{mn}^l(\pi/2)$.

Consider the correlation function between a spherical function f

under rotation $R(\alpha,\beta,\gamma)$ and another spherical function g:

$$c(\alpha,\beta,\gamma) := \sum_{l=0}^{l_{\max}} \sum_{m=-l}^{l} f_l^m(\alpha,\beta,\gamma) g_l^m.$$

The Wigner-D matrix leverages the decomposition in Eq. (7) and computes $c(\alpha,\beta,\gamma)$ at even samples of α, β, γ using an approach that is similar to fast Fourier transform:

$$\begin{aligned} c(\alpha,\beta,\gamma) &= \sum_{l,m,h,n} d^l_{mh} d^l_{hn} f_l^n g_l^m \exp\big(i(m\xi + h\eta + n\omega)\big) \\ &= \sum_{m,h,n} T(m,h,n) \exp\big(i(m\xi + h\eta + n\omega)\big) \end{aligned}$$

where $T(m,h,n) = \sum_l d^l_{mh} d^l_{hn} f_l^n g_l^m$. It can be accelerated by an inverse fast Fourier transform.

However, this Wigner-D matrix representation is still expensive to compute when the sampling density is high. One way to address the issue of running time is to leverage GPU, e.g., using the rotated zonal harmonic basis (RZHB) [NSF12]. This paper looks at this problem from the perspective of numerical optimization. In particular, when having a good initial rotation, which we will see how to predict using a low-resolution Wigner-D, we only need derivatives of $f_l^m(R)$ with respect to R to refine the rotation. The next section presents a result that shows that these derivatives have highly simple and sparse expressions.

5. Jacobian of Rotating Spherical Harmonics

In continuous optimization, for example, using the Gauss-Newton method, we only need the Jacobian of $f_l^m(R)$ with respect to R in the 3×3 identity matrix I_3. This section shows that this Jacobian can be described using a constant sparse matrix, greatly facilitating local optimization of R. Relevant developments include [KKP*06, MMBP22], which compute the derivatives of $f_l^m(R)$ under the Euler angle representation in Eq. (4). However, their methods are rather recursive. In contrast, we present the explicit formulation under the angle-axis representation, which is simple.

Our main result of this section is an expression of $Y_l^m(\theta+d\theta,\phi+d\phi)$ as linear combinations of $Y_l^m(\theta,\phi)$ where $d\theta$ and $d\phi$ are incurred by a rotation $R \approx I_3$. To this end, we need a parametrization of R in this neighborhood of I_3, which is given by

$$R \approx I_3 + \begin{pmatrix} 0 & -v_z & v_y \\ v_z & 0 & -v_x \\ -v_y & v_x & 0 \end{pmatrix}. \tag{8}$$

Next, we describe the relation between $d\theta$ and $d\phi$ with (v_x,v_y,v_z). Locally, the spherical point $(x,y,z) = (\sin\theta\cos\phi, \sin\theta\sin\phi, \cos\theta)$ will be transformed to $(x',y',z') = (\sin(\theta+d\theta)\cos(\phi+d\phi), \sin(\theta+d\theta)\sin(\phi+d\phi), \cos(\theta+d\theta))$ where

$$x' = x + v_y z - v_z y, \quad y' = y + v_z x - v_x z, \quad z' = z + v_x y - v_y x.$$

This leads to the following proposition.

Proposition 1 We have

$$d\theta = v_y\cos\phi - v_x\sin\phi, \quad d\phi = v_z - \frac{\cos\theta}{\sin\theta}\big(v_x\cos\phi + v_y\sin\phi\big).$$

Proof See Appendix A. □

Now we are ready to present our result on the expression of $Y_l^m(\theta+d\theta,\phi+d\phi)$ as linear combinations of $Y_l^m(\theta,\phi)$.

Theorem 1 Introduce

	$m=0$	$m=1$	$m>1$
$a_l^m =$	$\sqrt{\frac{(l+1)l}{2}}$	$\sqrt{\frac{(l+m+1)(l-m)}{2}}$	$\frac{\sqrt{(l+m+1)(l-m)}}{2}$
$b_l^m =$	0	$\sqrt{\frac{(l)(l+1)}{2}}$	$\frac{\sqrt{(l-m+1)(l+m)}}{2}$

Then,

$$\begin{aligned} &Y_l^m(\theta+d\theta,\phi+d\phi) - Y_l^m(\theta,\phi) = v_z(-mY_l^{-m}(\theta,\phi)) \\ &+ v_x\Big(a_l^{|m|}Y_l^{-m-\mathrm{sign}(m)}(\theta,\phi) + b_l^{|m|}Y_l^{-m+\mathrm{sign}(m)}(\theta,\phi)\Big) \\ &+ v_y\Big(-a_l^{|m|}Y_l^{m+\mathrm{sign}(m)}(\theta,\phi) + b_l^{|m|}Y_l^{m-\mathrm{sign}(m)}(\theta,\phi)\Big). \end{aligned} \tag{9}$$

where $\mathrm{sign}(0)=0$; $\mathrm{sign}(m)=1$ when $m>0$; $\mathrm{sign}(m)=-1$ when $m<0$; $Y_i^j(\theta,\phi)=0$ where $|j|>i$.

Proof See Appendix B. □

Theorem 1 suggests the following simple expression of coefficients of spherical harmonics when rotating a spherical function. Denote $f_l(R) = (f_l^{-l}(R);\cdots,f_l^l(R))$ as the l-th coefficient vector of a spherical function under rotation R. When R is approximated according to Eq. (8), we have

$$f_l(R) \approx (I + v_x A_l^x + v_y A_l^y + v_z A_l^z) f_l \tag{10}$$

where A_l^x, A_l^y, and A_l^z are constant sparse matrices whose elements are given by $a_l^{|m|}$ and $b_l^{|m|}$.

6. Stability Analysis

This section studies the magnitudes of the spherical harmonic coefficients of spherical functions that have self-symmetries. We show that in the presence of certain discrete symmetry groups in 3D, the coefficients of certain frequencies are zero. An important implication is that when aligning shapes perturbed from the same shape that has such symmetry groups, we should avoid aligning coefficients of these frequencies that correspond to noise. An analysis supporting this claim is presented in Appendix E.

To gain some intuition about the connections between symmetries and Fourier coefficients, let us first look at circular functions in 2D. Suppose a circular function $f:[0,2\pi)\to\mathbb{R}$ is k-way symmetric, i.e., $f(\phi+\frac{2j\pi}{k}) = f(\phi), \forall\phi\in[0,\frac{2\pi}{k}), 1\le j<k$. Consider its Fourier coefficients

$$\begin{aligned} f_{2i-1} &= \frac{1}{2\pi}\int_0^{2\pi} f(\phi)\cos(i\phi)f(\phi)d\phi, \\ f_{2i} &= \frac{1}{2\pi}\int_0^{2\pi} f(\phi)\sin(i\phi)f(\phi)d\phi. \end{aligned}$$

Proposition 2 if f is k-way symmetric, then $\forall i, \mathrm{mod}(i,k)\neq 0$,

$$f_{2i-1} = f_{2i} = 0.$$

Proof See Appendix C. □

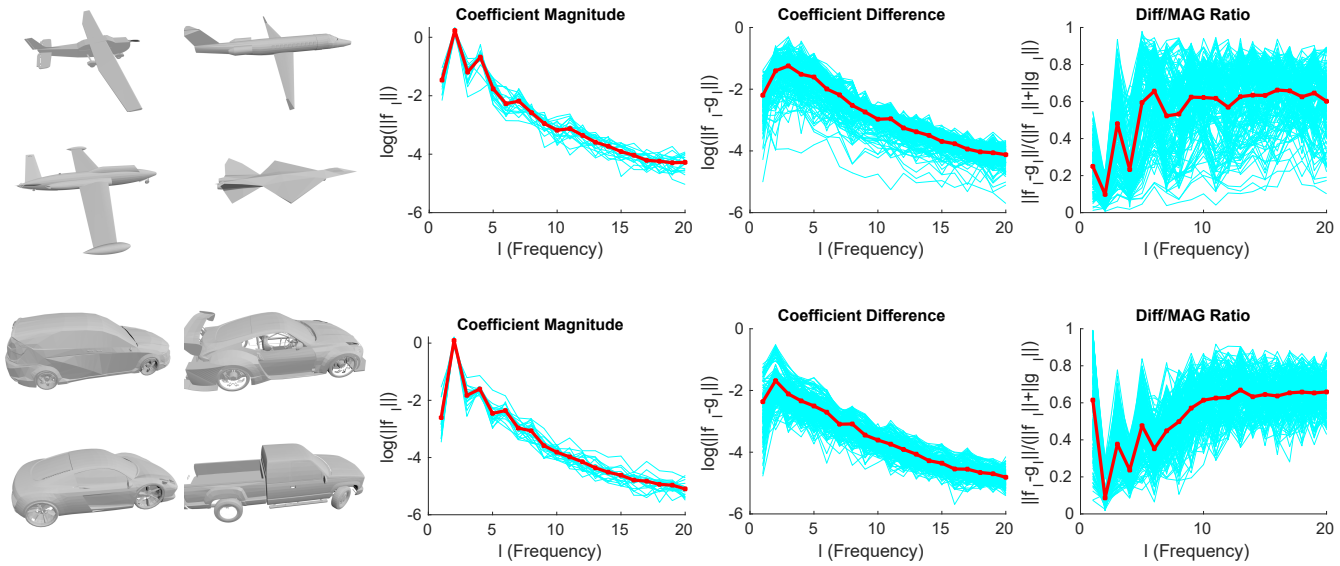

Figure 3: *We show deviations of spherical harmonics coefficients of signed-distance functions on a sphere around a collection of shapes. We show the spherical function of the largest radius defined in Figure 7.1. Two collections are shown here, each of which has 20 shapes and $l \leq 20$. (a) Samples of each collection. (b) Magnitudes of* $\log(\|f_l\|)$ *among the entire shape collection. Mean is bold-faced. (c) Magnitudes of* $log10.1145/2602161.2602167(\|f_l - g_l\|)$ *among all pairs of shapes. Mean is bold-faced (d) Ratios* $\frac{2\|f_l - g_l\|}{\|f_l\|+\|g_l\|}$. *Mean is bold-faced.*

The cases in 3D are more complicated. Let vector $f_l = (f_l^{-l}, \cdots, f_l^l)^T \in \mathbb{R}^{2l+1}$ collect all Fourier coefficients in order l. Our main result is described below.

Theorem 2 Let G be a discrete 3D symmetry group, namely, a finite subgroup of SO(3). A spherical function f is invariant under its group action if $\forall g \in G$, $f(g \cdot \mathbf{x}) = f(\mathbf{x})$. For a function f invariant under one of the five types of finite subgroups of SO(3), its spherical harmonic coefficients f_l can only be non-zero in the following cases

	Group type	Non-zero coefficients $f_l \neq 0$
C_n	Cyclic group	All $l \in \mathbb{N}$
D_n	Dihedral group	$l \equiv 0 \mod 2$
T	Tetrahedral group	$l \in \{0,3,4,6,7,9,10,\cdots\}$
O	Octahedral group	$l \in \{0,4,6,8,10,12,\cdots\}$
I	Icosahedral group	$l \in \{0,6,10,12,15,16,18,20,\cdots\}$

All other spherical harmonic coefficients not listed in this table vanish under the respective symmetries.

Proof See Appendix D. □

Define the ratio

$$s(f_l, g_l) = \frac{\|f_l - g_l\|}{\|f_l\| + \|g_l\| + \epsilon} \tag{11}$$

where $\epsilon = 10^{-10}$. This offset ϵ is introduced to ensure that the denominator does not incur numerical errors under exact symmetries under the conditions of Table 2. In practice, the objects we encounter do not have perfect rotational symmetries, and their SH coefficients do not vanish. However, we still observe certain vanishing effects in SH coefficients among many categories (see Figure 3(a)).

Specifically, Figure 3(b) shows that the norms of the SH coefficients do vibrate (small-large-small) among the first few frequencies, as the underlying shapes in Car and Airplane have approximate D_4 symmetries. Moreover, although $\|f_l - g_l\|$ decreases when increasing l (see Figure 3(c)), $s(f_l, g_l)$ exhibits exhibits desired properties. As shown in Figure 3(d), for both Airplane and Car, $l = 2$ has the smallest ratio, and the next smallest ratio is at $l = 4$. Their behaviors at $l = 1$ are different. We will use these patterns to design weighting functions that are used in aligning spherical harmonic coefficients.

In Section 7.1 and Section 7.3, we show how to weight SH coefficients for global initialization and local refinement, respectively.

7. Approach

This section presents details of our three-stage relative rotation estimation approach. In Section 7.1, we discuss how to pre-process the input shapes P and Q into a sequence of spherical functions $f^{P,i}$ and $f^{Q,i}$. In Section 7.2, we describe the second stage, which extracts a candidate set of rotations of Eq. (1) evaluated at a sparse set of rotation samples. They are calculated from a low-resolution Wigner-D matrix. With $\mathcal{R}_{in} \subset \mathrm{SO}(3)$ we denote the set of candidate rotations obtained from stage two. In Section 7.3, we introduce the final stage that performs the local optimization of Eq. (1), starting from each candidate rotation $R \in \mathcal{R}_{in}$. Our algorithm returns the best solution to the global objective function in the final stage.

7.1. Pre-processing

We define $f^{P,i}$ and $f^{Q,i}$ using signed distance functions of P and Q. Denote $d_P(x,y,z) : \mathbb{R}^3 \to \mathbb{R}$ as the signed distance from P at (x,y,z).

Under spherical coordinates, $f^{P,i}$ at radius r_i is given by

$$f^{P,i}(\theta,\phi) = d_P\big(r_i \sin\theta\cos\phi, r_i \sin\theta\cos\phi, r_i\cos\theta\big). \quad (12)$$

$f^{Q,i}$ is defined similarly. We choose $r_i, 1 \le i \le n_r = 5$ uniformly from $r_{\min} = 0.5$ to $r_{\max} = 2$

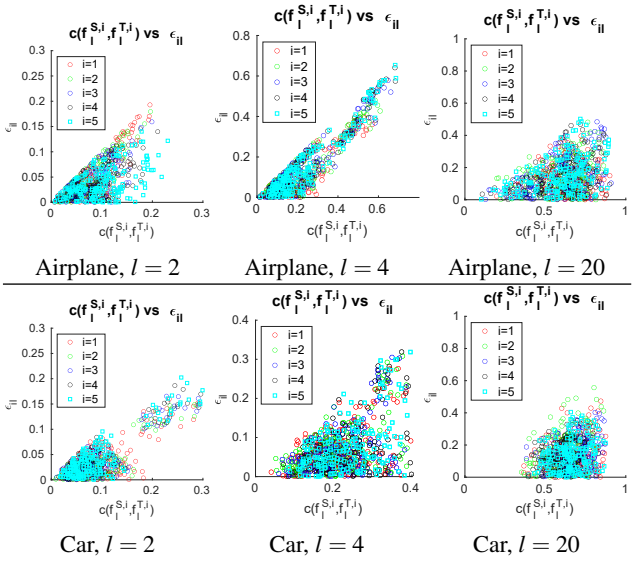

Figure 4: *We show correlations between $s(f_l^{P,i}, f_l^{Q,i})$ and ϵ_{il} for different l. We can see that they are correlated when $l = 2$ and $l = 4$, i.e., when $\|f_l^{P,i}\|$ and $\|f_l^{Q,i}\|$ are large. The correlations reduce when these two norms are small.*

We proceed to determine w_{il} in Eq. (1) for the global rotation initialization phase. As we do not know the underlying rotation between $f^{P,i}$ and $f^{Q,i}$, we find that we can use $\|f_l^{P,i}\|$ and $\|f_l^{Q,i}\|$, which are invariant when rotating $f^{P,i}$ and $f^{Q,i}$, to approximate $s(f_l^{P,i}, f_l^{Q,i})$. Introduce

$$\epsilon(f_l^{P,i}, f_l^{G,i}) = \frac{|\|f_l^{P,i}(I_3)\| - \|f_l^{Q,i}\||}{\|f_l^{P,i}(I_3)\| + \|f_l^{Q,i}\|}.$$

Figure 4 plots $\epsilon(f_l^{P,i}, f_l^{G,i})$ and $s(f_l^{P,i}, f_l^{Q,i})$ for different i and l in the Airplane and Car datasets shown in Figure 3. We can see that when the norms of $\|f_l^{P,i}\|$ and $\|f_l^{Q,i}\|$ are large (i.e., when they provide effective constraints on the underlying rotation), the value of $\epsilon(f_l^{P,i}, f_l^{G,i})$ offers a good approximation of $s(f_l^{P,i}, f_l^{Q,i})$. In light of this observation, we use $\epsilon(f_l^{P,i}, f_l^{G,i})$ to define

$$w_{il} = \exp\Big(-\frac{\epsilon(f_l^{P,i}, f_l^{G,i})^2}{2\sigma^2}\Big), \quad (13)$$

where we set $\sigma = 0.5$ in all of our experiments. In other words, we assign a very small weight when ϵ_{il} is large.

7.2. Initial Rotation Estimation

Our goal is to compute a candidate set of initial rotations $\mathcal{R}_{in}$ that approximate strong local minima of $e(R)$ in Eq. (1), where w_{il} is given by Eq. (13) and is independent of the target rotation. Note that

$$e(R) = \sum_{i=1}^{n_r}\sum_{l=1}^{l_{\max}} w_{il}\Big(\|f_l^{P,i}(I_3)\|^2 + \|f_l^{Q,i}\|^2\Big) - 2c(R) \quad (14)$$

where

$$c(R) = \sum_{i=1}^{n_r}\sum_{l=1}^{l_{\max}} w_{il} f_l^{P,i}(R)^T f_l^{Q,i}.$$

Using the Wigner-D matrix representation described in Section 4.2, we can compute $c(R(\alpha,\beta,\gamma))$ on uniform samples of α, β, and γ. This leads to values of $e(R)$ in the corresponding rotation samples. In our implementation, we place $n_\alpha = 24$ samples in α, $n_\gamma = 24$ samples in γ, and $n_\beta = 12$ samples in β. In other words, the angle between adjacent samples is 15° in α, β, and γ.

To detect strong local minima of $e(R)$, we find $(\alpha_i,\beta_i,\gamma_i)$ where $e(R(\alpha_i,\beta_i,\gamma_i))$ is a local minimum among the 27 neighbors of $(\alpha_i,\beta_i,\gamma_i)$. In the remainder of this paper, we will call them *discrete local minima*. These discrete local minima, which are computed at a coarse resolution, essentially remove weak local minima. On the other hand, they are inaccurate as they are on the grid.

We present a rectification step to improve the initial rotation estimations. For each discrete local minimum $(\alpha_i,\beta_i,\gamma_i)$, we parameterize R locally as $\exp(v\times)R(\alpha_i,\beta_i,\gamma_i)$ and approximate $e(R)$ locally using a quadratic function

$$\hat{e}(v,A) = e(R(\alpha_i,\beta_i,\gamma_i)) + v^T b + \frac{1}{2}v^T A v,$$

where b is given by $\frac{\partial e(R)}{\partial v}$ and can be computed by substituting Eq. (10) into Eq. (1). Given b, we compute the symmetric matrix A by solving the following optimization problem

$$\min_A \sum_{(\alpha_j,\beta_j,\gamma_j)\in\mathcal{N}(\alpha_i,\beta_i,\gamma_i)} \big(\hat{e}(v_{ij},A) - e(R(\alpha_j,\beta_j,\gamma_j))\big)^2, \quad s.t.\ A \succeq 0,$$

where $\mathcal{N}(\alpha_i,\beta_i,\gamma_i)$ collects six neighboring samples of $(\alpha_i,\beta_i,\gamma_i)$ (two in each axis of α, β, and γ), and v_{ij} is defined as

$$\exp(v_{ij}\times) = R(\alpha_j,\beta_j,\gamma_j)R(\alpha_i,\beta_i,\gamma_i)^T.$$

With this setup, we compute the correction

$$v = -A^\dagger b, \quad (15)$$

and augment $\mathcal{R}_{\text{init}}$ with $\exp(v\times)R(\alpha_i,\beta_i,\gamma_i)$.

7.3. Rotation Refinement

Starting from each $R_i \in \mathcal{R}_{in}$, the final stage of our approach performs local optimization to solve Eq. (1). In this local phase, we alternate between fixing w_{il} to optimize $e(R)$ and updating w_{il} from the current optimal solution R. When w_{il} are fixed, we employ the Gauss-Newton method with Levenberg–Marquardt iterative regularization to minimize $e(R)$. Denote R^c as the current rotation. Each Gauss-Newton step optimizes v by substituting (10) into (1)

$$\min_v \sum_{i=1}^{n_r}\sum_{l=1}^{l_{\max}} \|(I + v_x A_l^x + v_y A_l^y + v_z A_l^z) f_l^{P,i}(R^c) - f_l^{Q,i}\|^2 + \mu\|v\|^2 \quad (16)$$

	Chair	Table	Plane	Bag	Cap	Earph.	Guitar	Knife	Lamp	Laptop	Motor.	Mug	Pistol	Rocket	Skateb.	Car	Mean	Timing
MICCAI05	6.40	16.6	16.4	10.5	24.5	9.49	8.43	19.2	24.2	7.55	4.83	8.99	6.33	18.3	8.63	4.12	12.15	0.67
TIP13	6.82	15.9	17.1	9.72	23.6	9.69	8.72	19.3	24.1	7.58	4.93	8.91	6.25	18.4	8.43	3.92	12.08	0.83
PAMI07	7.06	16.3	16.8	10.9	23.8	9.59	8.83	19.6	24.4	7.75	4.93	9.03	6.47	18.5	8.79	4.21	12.31	0.46
JVCIR16	6.73	19.6	11.49	11.03	18.1	9.89	7.73	21.6	26.7	10.8	6.68	6.93	8.16	23.6	10.5	7.36	12.93	0.81
IROS18	24.3	24.5	25.3	25.8	47.2	14.9	15.3	31.4	42.1	15.4	14.6	31.2	14.1	29.9	28.2	19.5	25.23	0.11
4PCS+ICP	14.3	43.5	22.3	27.8	53.2	12.9	13.6	33.2	46.3	14.1	12.4	29.2	11.1	33.9	29.2	17.5	25.91	2.12
Ours	5.75	11.4	5.07	7.45	14.0	5.00	3.73	15.0	18.7	7.45	4.90	4.30	6.13	13.2	4.97	1.93	8.06	0.81
No-Weighting	6.50	16.4	16.8	10.9	24.2	9.59	8.12	21.2	23.2	7.83	4.98	8.91	6.16	18.6	8.59	3.97	12.25	0.80
No-LocalOpt	15.5	15.2	13.5	11.9	18.2	12.1	7.99	17.2	26.7	10.5	8.54	17.5	9.92	17.2	8.57	7.54	13.63	0.35
$n_\beta = 6$	6.65	11.7	5.74	7.97	15.3	6.12	4.27	16.1	19.3	7.88	5.11	6.72	6.52	13.6	5.23	2.15	8.77	0.76
$n_\beta = 24$	5.93	11.4	5.24	7.46	14.2	5.87	3.82	15.1	18.9	7.45	4.94	4.41	6.16	13.3	5.04	2.02	8.20	1.16
No-Refine	6.23	12.4	5.91	8.13	14.7	6.12	3.94	16.7	20.1	7.93	4.98	4.87	6.65	13.7	5.25	2.32	8.74	0.96
Top-1	12.3	41.2	20.8	25.8	46.2	6.86	6.46	35.2	40.3	8.01	5.41	20.2	7.12	36.9	26.2	13.5	22.03	0.48
Top-2	6.23	14.6	6.62	7.93	16.3	5.49	4.07	16.5	22.5	7.54	4.99	5.23	6.20	19.2	8.65	4.01	9.35	0.66
DGrid	5.41	16.2	13.9	12.9	20.4	9.72	10.1	16.2	21.3	7.45	4.23	9.21	7.49	15.1	8.57	4.36	11.4	4.07

Table 1: *This table presents quantitative results on ShapeNetPart, including rotation error for each category and the average running time for each shape pair. The top block shows results of five baselines. These include [HSZ*05] and [AMV13] that align the original spherical harmonics, and [Kaz07], [BHACB16], and [HTB18] that perform various approximations. The second block shows the result of our method. The third block shows an ablation study. (No-Weighting): Dropping the weights w_{il} in each term in Eq. (1). (No-Refine): Merely using the discrete local minima from the rotation samples. ($n_\beta = 6$): Using a coarse grid for rotation samples. ($n_\beta = 24$): Using a fine grid for rotation samples. (No-LocalOpt): Without local refinement. (Top-1): Using the best discrete local minimum for local refinement. (Top-2): Using the top two discrete local minima for local refinement. (DGrid): Using a dense grid to search the best rotation with weights in Eq. (13).*

where μ is the Levenberg–Marquardt regularization coefficient. The optimal v in (16) is given by

$$v^\star = \Big(\sum_{i=1}^{n_r}\sum_{l=1}^{l_{\max}} J_{l,i}^{c\,T} J_{l,i}^c + \mu I_3\Big)^{-1} \sum_{i=1}^{n_i}\sum_{l=1}^{l_{\max}} J_{l,i}^{c\,T}\big(f_l^{Q,i} - f_l^{P,i}(R^c)\big) \quad (17)$$

where

$$J_{l,i}^c = (A_l^x f_l^{P,i}(R^c), A_l^y f_l^{P,i}(R^c), A_l^z f_l^{P,i}(R^c)).$$

We then update R^c as $\exp(v^\star)R^c$. We dynamically adjust the value of μ to ensure that the objective function in Eq. (1) decreases during the optimization procedure. In our experiments, we find that in most cases $\mu = 0$ is sufficient. We only have a positive μ in cases where there are large shape variations between P and Q.

Given the current R^c, we compute

$$s_{il}^c = \frac{\|f_l^{P,i}(R^c) - f_l^{Q,i}\|}{\|f_l^{P,i}(I_3)\| + \|f_l^{Q,i}\|},$$

and set $w_{il} = \exp\big(-\frac{s_{il}^{c\,2}}{2\sigma^2}\big)$. In Section F, we present a local convergence analysis of the proposed alternating scheme.

8. Experimental Results

This section presents experimental evaluations of our approach. We begin with the experimental setup in Section 8.1. We then present an analysis of the experimental results in Section 8.2. Section 8.3 describes an ablation study.

8.1. Experimental Setup

We tested our algorithm in 16 popular categories of ShapeNetPart [YKC*16]. For each category, we randomly sample 20 shapes and evaluate the mean rotation error of each approach among all pairs of shapes. Most of these categories have global rotation symmetries. When evaluating rotation errors on them, we manually annotate the underlying symmetries and factor them out before calculating the rotation error. Let $\mathcal{R}_{\text{sym}}$ collect the rotations in a symmetry group, i.e., $|\mathcal{R}_{\text{sym}}| > 1$ iff there is a global rotation symmetry. Denote R_{PQ} and R_{PQ}^{gt} as the predicted and ground-truth relative rotation from a shape P to a shape Q, respectively. We compute the rotation error θ_{PQ} between them as

$$\theta_{PQ} = \min_{R\in\mathcal{R}_{\text{sym}}} \operatorname{acos}\left(\frac{\operatorname{tr}\left(R_{PQ}^T R R_{PQ}^{gt}\right) - 1}{2}\right),$$

which is the minimal rotation angle between the predicted relative rotation and the ground-truth relative rotations defined by the symmetry group. We report the mean of θ_{PQ} between all pairs of shapes in each category.

Baseline comparisons employ five non-learning based approaches introduced in the literature, i.e., MICCAI05 [HSZ*05], TIP13 [AMV13], PAMI07 [Kaz07], JVCIR16 [BHACB16], and IROS18 [HTB18]. In particular, MICCAI05 and TIP13 seek to solve the global optimization problem Eq. (1) with uniform weights w_{il}. PAMI07, JVCIR, and IROS18 involve various approximations of Eq. (1). For fair comparisons, our approach and all baseline approaches share the same spherical harmonics encodings. In addition, we also include a registration-based baseline, which combines Super4PCS [MAM14] to predict global rotation, followed by ICP [BM92, SK21] for local refinement.

All experiments were conducted on a Desktop with 20-Core 2.4HZ GPU and 128G main memory. All implementations used MATLAB 2024B. No GPUs were used. For all of our experiments,

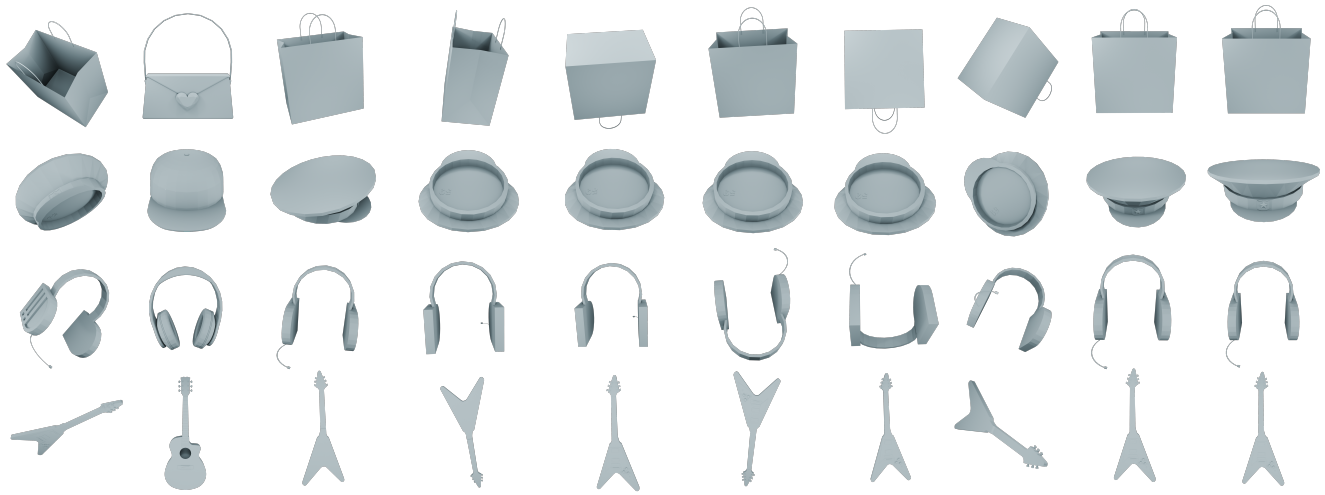

(a) Input (b) Target (c) MICCAI05 (d) TIP13 (e) PAMI07 (f) JVRIR16 (g) IROS18 (h) 4PCS+ICP (i) Ours (j) Source GT

Figure 5: *This figure shows qualitative results of baseline approaches and our approach. We show two challenging shape pairs. (a) Input source shape. (b) Target shape. (c) MICCAI05. (d) TIP13. (e) PAMI07. (f) JVRIR16. (g) IROS18. (h) 4PCS+ICP. (i) Ours. (j) Source shape with GT alignment.*

we used $l_{\max} = 20$ for all approaches except IROS18, which uses the leading SH coefficients.

8.2. Analysis of Results

Table 1 and Figure 5 show quantitative and qualitative results, respectively. In general, our approach outperforms all existing approaches in accuracy. The computational cost is on-par with efficient algorithms that use solve approximations of Eq. (1).

Compared to MICCAI05 and TIP13 which align SH coefficients directly, our approach improves from the best of them by 33.28% in mean rotation error. The main improvements come from the reweighting scheme that discards frequencies that contain a lot of noise due to rotation symmetries. We can see these effects on Table, Plane, Guitar, Knife, Motocycle, Rocket, Skateboard, and Car, which possess an approximate D_{2h} point group symmetry. The improvements in those are larger than those in other categories. Moreover, in the more challenging categories, such as Lamp and Pistol, the relative improvements are also salient. This shows the importance of aligning specific SH frequencies rather than all frequencies. Computationally, our approach has a running time similar to that of MICCAI05 and TIP13. The major improvements come from the efficient local refinement step, although we perform local optimization from multiple initial rotations. Figure 5 shows that our approach is more accurate than MICCAI05 and TIP13 both globally and locally, in which the reweighted objective function offers improved global and local minima.

Compared to PAMI07, JVCIR16, and IROS18 that align SH coefficients approximately, our approach shows significant improvements in rotation errors. Our approach is eight times slower than IROS18, which uses only the first three frequencies of the spherical harmonics. However, in terms of rotation errors, our approach is three times smaller, showing a significant improvement in accuracy. Our approach is about 80% times slower than PAMI07, but we improve from PAMI07 by 34.52% in terms of rotation errors. These results show that it is important to utilize all SH coefficients for rotation estimation and doing so directly, e.g., unlike the sequential approach of estimating rotation axis and rotation angle in order. Such improvements can be seen visually in Figure 5, in which PAMI07, JVCR16, and IROS18 exhibit various global errors.

The approach of matching feature points and then applying ICP refinement does not perform well. This approach is most suited for shapes that are very similar to each other and does not offer accurate results when the input shapes are very different from each other. Quantitatively, the accuracy is similar to the weakest baseline that aligns SH coefficients for relative rotation estimation. In terms of computational cost, feature matching is also more costly. On the other hand, feature matching is applicable for partial shape matching.

8.3. Ablation Study

This section presents an ablation study of our approach.

No-Weighting. In this setting, we eliminate weighting schemes in both the global optimization phase and the local refinement phase, i.e., $w_{il} = 1$ in Eq. (1). As shown in Table 1, the mean rotation error increases by 51.99% when using identical weights $w_{il} = 1$. The performance is still slightly better than that of MICCAI05 and TIP13 because we perform local refinement from multiple initial rotations. These results show that applying suitable weights to different frequencies is critical to improving the accuracy of rotation estimation.

No-LocalOpt. In this setting, we drop the local refinement step. This means that the final result is given solely by the rectification described in Eq. (15). Without local refinement, the mean ratio error increases by 69.35%. In addition to the fact that local refinement improves the local accuracy, we also find that it affects the final output. This is because the scores of the optimized rotations may be different from the initial rotations. An example of this is shown in the second column of Figure 5.

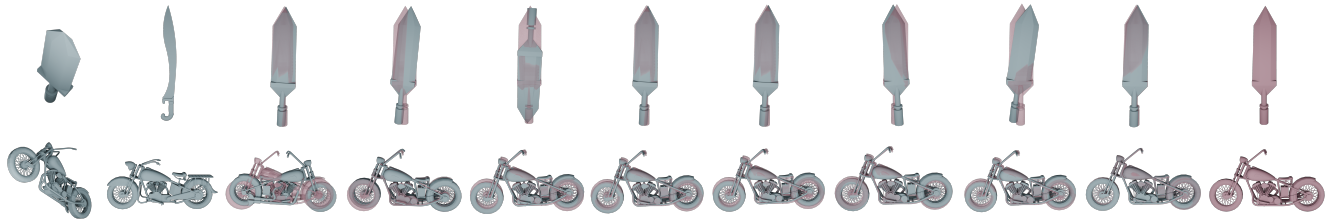

(a) Input (b) Target (c) NoWeig. (d) NoLocal. (e) $n_\beta = 6$ (f) $n_\beta = 24$ (g) NoRefine (h) Top-1 (i) Top-2 (j) Ours (k) Source GT

Figure 6: *This figure shows qualitative results of the ablation study. We show two representative shape pairs. (a) Input Source shape. (b) Target shape. (c) Without the reweighing scheme. (d) No local optimization. (e) $n_\beta = 6$ in the global rotation initialization phase. (f) $n_\beta = 24$ in the global rotation initialization phase. (g) No rectification when doing the initialization. (h) Using the top local minimum. (i) Using the top two local minima. (j) Our approach with default hyper-parameters. (k) Source shape with GT alignment. Source shapes with GT alignment are colored in red and overlaid with other results for better comparison.*

Grid resolution for initial rotation estimation. The default grid resolution is $n_\beta = 12$ for a grid of $24 \times 12 \times 24$ on which we compute the alignment scores. We have tested when setting $n_\beta = 6$ and $n_\beta = 24$. As shown in Table 1 and Figure 5, the mean rotation error increases by 8.81% when using $n_\beta = 6$. This can be understood as the fact that discrete local minima from a very coarse grid can be inaccurate, and this cannot be recovered from the rectification step in Eq. (15). Visually, using a coarse grid can lead to both local and global errors due to competing local minima. In contrast, using $n_\beta = 24$ leads to 67% increase in running time. In terms of precision, the mean rotation error also increases by 1.74%. An explanation is that there are many local minima when $n_\beta = 24$, and we may miss important ones by choosing the top-3 local minima.

No-Refinement. In this setting, we drop the local rectification step in Eq. (15) and start the local optimization from the discrete local minima directly. In this case, the running time increases by 20.5% as the local optimization step needs more iterations to converge. On the other hand, we also see that the mean rotation error increases slightly by 8.44%. This is caused by the fact that for challenging shape pairs, there are a lot of weak local minima near the global optimum. The rectification step can avoid such weak local minima using values of the objective function on neighboring samples. Without the rectification step, local optimization can get stuck in a weak local minimum near a discrete local minimum.

Varying the number of discrete local minima. Another hyper-parameter is how many discrete local minima (sorted in the increasing order of their objective values) to test for local optimization. When $n_\beta = 12$, the default value is 3. We tested using the top-1 and top-2 discrete local minima for local optimization. As shown in Table 1, only using the best discrete local minimum increases the mean rotation error by 273.3%. Using top-2 discrete local minima only increases the mean rotation error by 15.71%, a significant improvement over using the best. Visually, using a few local minima can miss the underlying global minimum, which cannot be recovered from local optimization. We also tested using top-4 discrete local minima, and the difference in mean ration error is about 0.3%, while the running time increases by 15%. This means that using the top-3 discrete local minima maintains a good balance between accuracy and efficiency.

Dense grid search. Another strategy is to apply the FFT step of our approach on a dense grid with $n_\beta = 96$ and return the optimal solution among the dense set of samples of SO(3) specified by grid vertices. This strategy is equivalent to applying the baseline MICCAI05 [HSZ*05] (top row of Table 1 on a dense grid with non-uniform weights. Denoted as DGrid in Table 1), this variant increases the computational cost by 400%. However, the accuracy also drops by noticeable margins. The reason is that the global phase does not have access to a better prediction of the term weights as we do not know the underlying relative pose.

9. Conclusions, Discussions, and Future Work

In this paper, we have introduced an approach to compute the relative rotation between two normalized shapes by converting them into spherical functions and solving an optimization problem that minimizes the differences between their rotated coefficients of spherical harmonics. The objective function is based on a stability analysis showing that, due to symmetries, the coefficients of some frequencies are more useful than others. This leads to a robust objective function whose global minimums are more meaningful than the widely used squared sum of L2 distances between coefficients of all frequencies. We introduce a numerical optimization scheme to solve the induced optimization problem. Experimental results show that our approach outperforms baseline approaches both qualitatively and quantitatively.

From an optimization perspective, the search space is only three-dimensional. Even with such a low-dimensional optimization problem, our experiments show that the loss surface can be very complicated. The problems are two-fold. The first is that there are many local minima. The second issue is that the local minima may be inaccurate. What we find in our experiments is that these two issues are competing, meaning a smooth loss surface tends to have fewer local minima, while the global minimum of a sharp loss surface (e.g., when using a robust norm) is more accurate, but it may have many local minima. The way we address this issue is to use discrete local minima at a coarse resolution and a rectification step that does implicit smoothing.

Besides serving as a relation rotation estimation approach, the research results in this paper open the door to developing a 3D neural representation using spherical harmonics. In particular, we can use the pose estimation approach in this paper to learn a spherical harmonic neural representation in a canonical coordinate system,

e.g., a generative model that maps latent codes to spherical harmonic coefficients. During training/testing, we can optimize the rotation of each instance together with this generative model, in which the local optimization step plays a very important role. The advantage of aligning spherical harmonics in a canonical coordinate system is to avoid constructing an equivariant/invariant network using the expensive Wigner-D representation. Intuitively, this avoids the Wigner-D representation being applied repeatedly to factor out the same rotation that is shared by all the layers.

Acknowledgment. This project was supported by NSF IIS-2047677, NSF IIS-2413161, the Toyota Research Institute University 2.0 Program, ARL grant W911NF-21-2-0104, a Vannevar Bush Faculty Fellowship, and Gifts from Adobe, Google and the Flexiv corporation. We also thank Peng Shan, Wenbin Yan, and Dali Cheng for their discussions on group theory.

References

[AB63] ALTMANN S. L., BRADLEY C. J.: On the symmetries of spherical harmonics. *Philosophical Transactions of the Royal Society of London. Series A, Mathematical and Physical Sciences 255*, 1054 (1963), 199–215. 3

[AGSL19] AOKI Y., GOFORTH H., SRIVATSAN R. A., LUCEY S.: Pointnetlk: Robust & efficient point cloud registration using pointnet. In *IEEE Conference on Computer Vision and Pattern Recognition, CVPR 2019, Long Beach, CA, USA, June 16-20, 2019* (2019), Computer Vision Foundation / IEEE, pp. 7163–7172. URL: http://openaccess.thecvf.com/content_CVPR_2019/html/Aoki_PointNetLK_Robust__Efficient_Point_Cloud_Registration_Using_PointNet_CVPR_2019_paper.html. 2

[Ale22] ALEXA M.: Super-fibonacci spirals: Fast, low-discrepancy sampling of SO(3). In *IEEE/CVF Conference on Computer Vision and Pattern Recognition, CVPR 2022, New Orleans, LA, USA, June 18-24, 2022* (2022), IEEE, pp. 8281–8290. URL: https://doi.org/10.1109/CVPR52688.2022.00811. 2

[AMC08] AIGER D., MITRA N. J., COHEN-OR D.: 4-points congruent sets for robust pairwise surface registration. *ACM Trans. Graph. 27*, 3 (2008), 85. URL: https://doi.org/10.1145/1360612.1360684. 2

[AMV13] ALTHLOOTHI S., MAHOOR M. H., VOYLES R. M.: A robust method for rotation estimation using spherical harmonics representation. *IEEE Trans. Image Process. 22*, 6 (2013), 2306–2316. URL: https://doi.org/10.1109/TIP.2013.2249083. 8

[BC10] BRADLEY C. J. C. J., CRACKNELL A. P.: The mathematical theory of symmetry in solids : representation theory for point groups and space groups, 2023 - 2010. 3

[BH95] BUREL G., HENOCQ H.: Determination of the orientation of 3D objects using spherical harmonics. *CVGIP Graph. Model. Image Process. 57*, 5 (1995), 400–408. URL: https://doi.org/10.1006/gmip.1995.1034. 3, 4

[BHACB16] BENSEDDIK H.-E., HADJ-ABDELKADER H., CHERKI B., BOUCHAFA S.: Direct method for rotation estimation from spherical images using 3D mesh surfaces with spharm representation. *Journal of Visual Communication and Image Representation 40* (October 2016), 708–720. 8

[BM92] BESL P. J., MCKAY N. D.: A method for registration of 3-d shapes. *IEEE Trans. Pattern Anal. Mach. Intell. 14*, 2 (1992), 239–256. URL: https://doi.org/10.1109/34.121791. 8

[BTP13] BOUAZIZ S., TAGLIASACCHI A., PAULY M.: Sparse iterative closest point. *Comput. Graph. Forum 32*, 5 (2013), 113–123. URL: https://doi.org/10.1111/cgf.12178. 2

[CHSA21] CAI R., HARIHARAN B., SNAVELY N., AVERBUCH-ELOR H.: Extreme rotation estimation using dense correlation volumes. In *IEEE Conference on Computer Vision and Pattern Recognition, CVPR 2021, virtual, June 19-25, 2021* (2021), Computer Vision Foundation / IEEE, pp. 14566–14575. URL: https://openaccess.thecvf.com/content/CVPR2021/html/Cai_Extreme_Rotation_Estimation_Using_Dense_Correlation_Volumes_CVPR_2021_paper.html. 2

[CIGR99] CHOI C. H., IVANIC J., GORDON M. S., RUEDENBERG K.: Rapid and stable determination of rotation matrices between spherical harmonics by direct recursion. *The Journal of Chemical Physics 111*, 19 (11 1999), 8825–8831. URL: https://doi.org/10.1063/1.480229. 3

[CMS87] CABRAL B., MAX N., SPRINGMEYER R.: Bidirectional reflection functions from surface bump maps. *SIGGRAPH Comput. Graph. 21*, 4 (Aug. 1987), 273–281. URL: https://doi.org/10.1145/37402.37434. 2

[CPK19] CHOY C. B., PARK J., KOLTUN V.: Fully convolutional geometric features. In *2019 IEEE/CVF International Conference on Computer Vision, ICCV 2019, Seoul, Korea (South), October 27 - November 2, 2019* (2019), IEEE, pp. 8957–8965. URL: https://doi.org/10.1109/ICCV.2019.00905. 2

[EAMD20] ESTEVES C., ALLEN-BLANCHETTE C., MAKADIA A., DANIILIDIS K.: Learning SO(3) equivariant representations with spherical cnns. *Int. J. Comput. Vis. 128*, 3 (2020), 588–600. URL: https://doi.org/10.1007/s11263-019-01220-1. 2, 3

[FRB08] FEHR J., REISERT M., BURKHARDT H.: Fast and accurate rotation estimation on the 2-sphere without correspondences. In *Computer Vision - ECCV 2008, 10th European Conference on Computer Vision, Marseille, France, October 12-18, 2008, Proceedings, Part II* (2008), Forsyth D. A., Torr P. H. S., Zisserman A., (Eds.), vol. 5303 of *Lecture Notes in Computer Science*, Springer, pp. 239–251. URL: https://doi.org/10.1007/978-3-540-88688-4_18. 1, 3

[Gre03] GREEN R.: Spherical harmonic lighting: The gritty details. In *Archives of the Game Developers Conference* (2003), vol. 56, p. 47. 2

[HGU*21] HUANG S., GOJCIC Z., USVYATSOV M., WIESER A., SCHINDLER K.: Predator: Registration of 3D point clouds with low overlap. In *IEEE Conference on Computer Vision and Pattern Recognition, CVPR 2021, virtual, June 19-25, 2021* (2021), Computer Vision Foundation / IEEE, pp. 4267–4276. URL: https://openaccess.thecvf.com/content/CVPR2021/html/Huang_Predator_Registration_of_3D_Point_Clouds_With_Low_Overlap_CVPR_2021_paper.html. 2

[HMR09] HOOVER R. C., MACIEJEWSKI A., ROBERTS R. G.: Pose estimation from images correlated on s1, s2, and so(3) using eigendecomposition in conjunction with spectral theory. *IEEE Transactions on Image Processing 18*, 11 (2009), 2562–2571. 1, 3

[HSZ*05] HUANG H., SHEN L., ZHANG R., MAKEDON F., HETTLEMAN B., PEARLMAN J. D.: Surface alignment of 3D spherical harmonic models: Application to cardiac MRI analysis. In *Medical Image Computing and Computer-Assisted Intervention - MICCAI 2005, 8th International Conference, Palm Springs, CA, USA, October 26-29, 2005, Proceedings, Part I* (2005), Duncan J. S., Gerig G., (Eds.), vol. 3749 of *Lecture Notes in Computer Science*, Springer, pp. 67–74. URL: https://doi.org/10.1007/11566465_9. 1, 3, 4, 8, 10

[HTB18] HADJ-ABDELKADER H., TAHRI O., BENSEDDIK H.: Closed form solution for rotation estimation using photometric spherical moments. In *2018 IEEE/RSJ International Conference on Intelligent Robots and Systems, IROS 2018, Madrid, Spain, October 1-5, 2018* (2018), IEEE, pp. 627–634. URL: https://doi.org/10.1109/IROS.2018.8593920. 3, 8

[IR98] IVANIC J., RUEDENBERG K.: Rotation matrices for real spherical harmonics. direct determination by recursion. *The Journal of Physical Chemistry A 102* (november 1998). 3, 4

[Kar07] KARNEY C. F.: Quaternions in molecular modeling. *Journal of Molecular Graphics and Modelling 25* (January 2007), 595–604. 2

[Kaz07] KAZHDAN M. M.: An approximate and efficient method for optimal rotation alignment of 3D models. *IEEE Trans. Pattern Anal. Mach. Intell. 29*, 7 (2007), 1221–1229. URL: https://doi.org/10.1109/TPAMI.2007.1032. 1, 2, 3, 8

[KCD*04] KAZHDAN M. M., CHAZELLE B., DOBKIN D. P., FUNKHOUSER T. A., RUSINKIEWICZ S.: A reflective symmetry descriptor for 3D models. *Algorithmica 38*, 1 (2004), 201–225. URL: https://doi.org/10.1007/s00453-003-1050-5. 3

[KFR03] KAZHDAN M., FUNKHOUSER T., RUSINKIEWICZ S.: Rotation invariant spherical harmonic representation of 3D shape descriptors. In *Proceedings of the 2003 Eurographics/ACM SIGGRAPH Symposium on Geometry Processing* (Goslar, DEU, 2003), SGP '03, Eurographics Association, p. 156–164. 2, 3

[KGC15] KENDALL A., GRIMES M., CIPOLLA R.: Posenet: A convolutional network for real-time 6-dof camera relocalization. In *2015 IEEE International Conference on Computer Vision, ICCV 2015, Santiago, Chile, December 7-13, 2015* (2015), IEEE Computer Society, pp. 2938–2946. URL: https://doi.org/10.1109/ICCV.2015.336. 2

[KKP*06] KRIVÁNEK J., KONTTINEN J., PATTANAIK S., BOUATOUCH K., ŽÁRA J.: Fast approximation to spherical harmonic rotation. In *Proceedings of the 22nd Spring Conference on Computer Graphics* (New York, NY, USA, 2006), SCCG '06, Association for Computing Machinery, p. 49–58 PAGE@9. URL: https://doi.org/10.1145/2602161.2602167, pathdoi:10.1145/2602161.2602167. 5

[KKP13] KAKARALA R., KALIAMOORTHI P., PREMACHANDRAN V.: Three-dimensional bilateral symmetry plane estimation in the phase domain. In *2013 IEEE Conference on Computer Vision and Pattern Recognition, Portland, OR, USA, June 23-28, 2013* (2013), IEEE Computer Society, pp. 249–256. URL: https://doi.org/10.1109/CVPR.2013.39. 3

[LJYL16] LI B., JOHAN H., YE Y., LU Y.: Efficient 3D reflection symmetry detection: A view-based approach. *Graph. Model. 83* (2016), 2–14. URL: https://doi.org/10.1016/j.gmod.2015.09.003. 3

[LWZ*19] LU W., WAN G., ZHOU Y., FU X., YUAN P., SONG S.: Deepvcp: An end-to-end deep neural network for point cloud registration. In *2019 IEEE/CVF International Conference on Computer Vision, ICCV 2019, Seoul, Korea (South), October 27 - November 2, 2019* (2019), IEEE, pp. 12–21. URL: https://doi.org/10.1109/ICCV.2019.00010. 2

[MAM14] MELLADO N., AIGER D., MITRA N. J.: Super 4PCS fast global pointcloud registration via smart indexing. *Comput. Graph. Forum 33*, 5 (2014), 205–215. URL: https://doi.org/10.1111/cgf.12446. 2, 8

[Mar72] MARSAGLIA G.: Choosing a point from the surface of a sphere. *The Annals of Mathematical Statistics 43* (1972), 645–646. 2

[MD06] MAKADIA A., DANIILIDIS K.: Rotation recovery from spherical images without correspondences. *IEEE Trans. Pattern Anal. Mach. Intell. 28*, 7 (2006), 1170–1175. URL: https://doi.org/10.1109/TPAMI.2006.150. 1, 3

[MGP06] MITRA N. J., GUIBAS L. J., PAULY M.: Partial and approximate symmetry detection for 3D geometry. *ACM Trans. Graph. 25*, 3 (2006), 560–568. URL: https://doi.org/10.1145/1141911.1141924. 2

[Mit08] MITCHELL J. C.: Sampling rotation groups by successive orthogonal images. *SIAM Journal on Scientific Computing 30* (2008), 525–547. 2

[MMBP22] MÉZIÈRES P., MELLADO N., BARTHE L., PAULIN M.: Recursive analytic spherical harmonics gradient for spherical lights. *Comput. Graph. Forum 41*, 2 (2022), 393–406. URL: https://doi.org/10.1111/cgf.14482, pathdoi:10.1111/CGF.14482. 5

[MPD06] MAKADIA A., PATTERSON A., DANIILIDIS K.: Fully automatic registration of 3D point clouds. In *2006 IEEE Computer Society Conference on Computer Vision and Pattern Recognition (CVPR 2006), 17-22 June 2006, New York, NY, USA* (2006), IEEE Computer Society, pp. 1297–1304. URL: https://doi.org/10.1109/CVPR.2006.122. 1, 3

[MS67] MACROBERT T. M., SNEDDON I. N.: *Spherical harmonics; an elementary treatise on harmonic functions with applications, third edition*. Methuen co. ltd., London, 1967. 2

[MSHS06] MARTINET A., SOLER C., HOLZSCHUCH N., SILLION F. X.: Accurate detection of symmetries in 3D shapes. *ACM Trans. Graph. 25*, 2 (Apr. 2006), 439–464. URL: https://doi.org/10.1145/1138450.1138462. 3

[MZA*18] MALLAHI M. E., ZOUHRI A., AFFAR A. E., TAHIRI A., QJIDAA H.: Radial hahn moment invariants for 2d and 3D image recognition. *Int. J. Autom. Comput. 15*, 3 (2018), 277–289. URL: https://doi.org/10.1007/s11633-017-1071-1. 3

[NSF12] NOWROUZEZAHRAI D., SIMARI P., FIUME E.: Sparse zonal harmonic factorization for efficient SH rotation. *ACM Trans. Graph. 31*, 3 (June 2012). URL: https://doi.org/10.1145/2167076.2167081, pathdoi:10.1145/2167076.2167081. 5

[PG21] POULENARD A., GUIBAS L. J.: A functional approach to rotation equivariant non-linearities for tensor field networks. In *IEEE Conference on Computer Vision and Pattern Recognition, CVPR 2021, virtual, June 19-25, 2021* (2021), Computer Vision Foundation / IEEE, pp. 13174–13183. URL: https://openaccess.thecvf.com/content/CVPR2021/html/Poulenard_A_Functional_Approach_to_Rotation_Equivariant_Non-Linearities_for_Tensor_Field_CVPR_2021_paper.html. 2, 3

[PMW*08] PAULY M., MITRA N. J., WALLNER J., POTTMANN H., GUIBAS L. J.: Discovering structural regularity in 3D geometry. *ACM Trans. Graph. 27*, 3 (2008), 43. URL: https://doi.org/10.1145/1360612.1360642. 2

[PRPO19] POULENARD A., RAKOTOSAONA M., PONTY Y., OVSJANIKOV M.: Effective rotation-invariant point CNN with spherical harmonics kernels. In *2019 International Conference on 3D Vision, 3DV 2019, Québec City, QC, Canada, September 16-19, 2019* (2019), IEEE, pp. 47–56. URL: https://doi.org/10.1109/3DV.2019.00015. 2, 3

[PTVF92] PRESS W. H., TEUKOLSKY S. A., VETTERLING W. T., FLANNERY B. P.: *Numerical recipes in C (2nd ed.): the art of scientific computing*. Cambridge University Press, USA, 1992. 4

[QYW*23] QIN Z., YU H., WANG C., GUO Y., PENG Y., ILIC S., HU D., XU K.: Geotransformer: Fast and robust point cloud registration with geometric transformer. *IEEE Trans. Pattern Anal. Mach. Intell. 45*, 8 (2023), 9806–9821. URL: https://doi.org/10.1109/TPAMI.2023.3259038. 2

[Ram02] RAMAMOORTHI R.: *A signal-processing framework for forward and inverse rendering*. PhD thesis, Stanford University, 2002. 2

[RK99] RITCHIE D. W., KEMP G. J. L.: Fast computation, rotation, and comparison of low resolution spherical harmonic molecular surfaces. *Journal of Computational Chemistry 20*, 4 (1999), 383–395. 3, 4

[RL18] REHMAN H. Z. U., LEE S.: Automatic image alignment using principal component analysis. *IEEE Access 6* (2018), 72063–72072. URL: https://doi.org/10.1109/ACCESS.2018.2882070. 2

[Rus07] RUSTAMOV R. M.: Augmented symmetry transforms. In *2007 International Conference on Shape Modeling and Applications (SMI 2007), 13-15 June 2007, Lyon, France* (2007), IEEE Computer Society, pp. 13–20. URL: https://doi.org/10.1109/SMI.2007.6. 3

[SAWG91] SILLION F. X., ARVO J. R., WESTIN S. H., GREENBERG D. P.: A global illumination solution for general reflectance distributions. In *Proceedings of the 18th Annual Conference on Computer Graphics and Interactive Techniques* (New York, NY, USA, 1991), SIGGRAPH '91, Association for Computing Machinery, p. 187–196. URL: https://doi.org/10.1145/122718.122739. 2

[SFM09] SHEN L., FARID H., MCPEEK M. A.: Modeling three-dimensional morphological structures using spherical harmonics. *Evolution 63*, 4 (2009), 1003–1016. URL:

https://onlinelibrary.wiley.com/doi/abs/10.1111/j.1558-5646.2008.00557.x. 3, 4

[SK21] SAHILLIOGLU Y., KAVAN L.: Scale-adaptive ICP. *Graph. Model. 116* (2021), 101113. URL: https://doi.org/10.1016/j.gmod.2021.101113, *path*doi:10.1016/J.GMOD.2021.101113. 8

[SKS09] SHEN L., KIM S., SAYKIN A. J.: Fourier method for large-scale surface modeling and registration. *Comput. Graph. 33*, 3 (2009), 299–311. URL: https://doi.org/10.1016/j.cag.2009.03.002. 3

[Slo08] SLOAN P.-P.: Stupid spherical harmonics (sh) tricks. In *Game Developers Conference* (feburary 2008). 2

[SWK07] SCHNABEL R., WAHL R., KLEIN R.: Efficient RANSAC for point-cloud shape detection. *Comput. Graph. Forum 26*, 2 (2007), 214–226. URL: https://doi.org/10.1111/j.1467-8659.2007.01016.x. 2

[TCL*13] TAM G. K. L., CHENG Z., LAI Y., LANGBEIN F. C., LIU Y., MARSHALL A. D., MARTIN R. R., SUN X., ROSIN P. L.: Registration of 3D point clouds and meshes: A survey from rigid to nonrigid. *IEEE Trans. Vis. Comput. Graph. 19*, 7 (2013), 1199–1217. URL: https://doi.org/10.1109/TVCG.2012.310. 2

[Tin03] TINKHAM M.: *roup Theory and Quantum MechanicsG*. Dover Publications, 2003. 2

[TSK*18] THOMAS N., SMIDT T. E., KEARNES S., YANG L., LI L., KOHLHOFF K., RILEY P.: Tensor field networks: Rotation- and translation-equivariant neural networks for 3D point clouds. *CoRR abs/1802.08219* (2018). URL: http://arxiv.org/abs/1802.08219. 2, 3

[WLH*23] WANG H., LIU Y., HU Q., WANG B., CHEN J., DONG Z., GUO Y., WANG W., YANG B.: Roreg: Pairwise point cloud registration with oriented descriptors and local rotations. *IEEE Trans. Pattern Anal. Mach. Intell. 45*, 8 (2023), 10376–10393. URL: https://doi.org/10.1109/TPAMI.2023.3244951. 2

[Wym04] WYMAN C. R.: *Fast local approximation to global illumination*. PhD thesis, The University of Utah, 2004. AAI3133130. 2

[YJLM10] YERSHOVA A., JAIN S., LAVALLE S. M., MITCHELL J. C.: Generating uniform incremental grids on *SO*(3) using the Hopf fibration. *Int. J. Robotics Res. 29*, 7 (2010), 801–812. URL: https://doi.org/10.1177/0278364909352700. 2

[YKC*16] YI L., KIM V. G., CEYLAN D., SHEN I.-C., YAN M., SU H., LU C., HUANG Q., SHEFFER A., GUIBAS L.: A scalable active framework for region annotation in 3D shape collections. *ACM Trans. Graph. 35*, 6 (Dec. 2016). URL: https://doi.org/10.1145/2980179.2980238. 2, 8

Appendix A: Proof of Prop. 1

Proof First,

$$-d\theta\sin(\theta)=\cos(\theta+d\theta)-\cos(\theta)=c_xy-c_yx=c_x\sin(\theta)\sin(\phi)-c_y\sin(\theta)\cos(\phi).$$

This means

$$d\theta=c_y\cos(\phi)-c_x\sin(\phi).$$

Moreover,

$$\begin{aligned}\cos(\phi)d\phi=&\sin(\phi+d\phi)-\sin(\phi)=\frac{c_zx-c_xz}{\sqrt{1-z^2}}+\frac{yz(c_xy-c_yx)}{\sqrt{(1-z^2)^3}}\\=&\frac{c_z\sin(\theta)\cos(\phi)-c_x\cos(\theta)}{\sin(\theta)}+\frac{\sin(\theta)\sin(\phi)\cos(\theta)(c_x\sin(\theta)\sin(\phi)-c_y\sin(\theta)\cos(\phi)}{\sin^3(\theta)}\\=&c_z\cos(\phi)-c_x\frac{\cos(\theta)(1-\sin^2(\phi))}{\sin(\theta)}-c_y\frac{\cos(\theta)\sin(\phi)\cos(\phi)}{\sin(\theta)}\\=&\cos(\phi)\big(c_z-\frac{\cos(\theta)}{\sin(\theta)}(c_x\cos(\phi)+c_y\sin(\phi))\big).\end{aligned}$$

This means $d\phi=c_z-\frac{\cos(\theta)}{\sin(\theta)}(c_x\cos(\phi)+c_y\sin(\phi))$, which ends the proof. □

Appendix B: Proof of Theorem 1

Applying Prop. 1, we have

$$\begin{aligned}Y_l^0(\theta+d\theta,\phi+d\phi)-Y_l^0(\theta,\phi)=&-K_l^0\frac{\partial P_l^0(\cos(\theta))}{\partial z}\sin(\theta)d\theta\\=&-K_l^0\big(c_y\cos(\phi)\frac{\partial P_l^0(\cos(\theta))}{\partial z}\sin(\theta)-c_x\sin(\phi)\frac{\partial P_l^0(\cos(\theta))}{\partial z}\sin(\theta)\big).\end{aligned}$$

Note that

$$\frac{\partial P_l^0(z)}{\partial z}=\frac{(-1)^l}{2^ll!}\frac{\partial^{l+1}(z^2-1)^l}{\partial^{l+1}z}.$$

More over

$$P_l^1(z)=\frac{(-1)^l}{2^ll!}(1-z^2)^{\frac{1}{2}}\frac{\partial^{l+1}(z^2-1)^l}{\partial^{l+1}z}.$$

This means

$$P_l^1(\cos(\theta))=\sin(\theta)\frac{\partial P_l^0(\cos(\theta))}{\partial z}.$$

It follows that

$$Y_l^0(\theta+d\theta,\phi+d\phi)=Y_l^0(\theta,\phi)+\frac{K_l^0}{\sqrt{2}K_l^1}(c_xY_l^{-1}(\theta,\phi)-c_yY_l^1(\theta,\phi))=Y_l^0(\theta,\phi)+\sqrt{\frac{l(l+1)}{2}}(c_xK_l^{-1}(\theta,\phi)-c_yK_l^1(\theta,\phi)).$$

Define for $m>1$,

$$Q_l^m(z)=\frac{1}{2}\big(\frac{mz}{\sqrt{1-z^2}}P_l^m(z)+\sqrt{1-z^2}\frac{\partial P_l^m(z)}{\partial z}\big),\tag{18}$$

$$R_l^m(z)=\frac{1}{2}\big(\frac{mz}{\sqrt{1-z^2}}P_l^m(z)-\sqrt{1-z^2}\frac{\partial P_l^m(z)}{\partial z}\big).\tag{19}$$

The first lemma expresses $Y_l^m(\theta+d\theta,\phi+d\phi)$ using $Y_l^m(\theta,\phi)$, $P_l^m(\cos(\theta))$, and $Q_l^m(\cos(\theta))$.

Lemma 1 For $m>0$, we have

$$\begin{aligned}Y_l^m(\theta+d\theta,\phi+d\phi)-Y_l^m(\theta,\phi)=&c_z(-mY_l^{-m}(\theta,\phi))+c_x\sqrt{2}K_l^m(\sin((m+1)\phi)Q_l^m(\cos(\theta))+\sin((m-1)\phi)R_l^m(\cos(\theta)))\\&+c_y\sqrt{2}K_l^m(-\cos((m+1)\phi)Q_l^m(\cos(\theta))+\cos((m-1)\phi)R_l^m(\cos(\theta)))\end{aligned}\tag{20}$$

and

$$Y_l^{-m}(\theta+d\theta,\phi+d\phi)-Y_l^{-m}(\theta,\phi) = c_z(mY_l^m(\theta,\phi)) + c_x\sqrt{2}K_l^m(-\cos((m+1)\phi)Q_l^m(\cos(\theta)) - \cos((m-1)\phi)R_l^m(\cos(\theta))) + c_y\sqrt{2}K_l^m(-\sin((m+1)\phi)Q_l^m(\cos(\theta)) + \sin((m-1)\phi)R_l^m(\cos(\theta))). \quad (21)$$

Proof See Section B. □

The following lemma characterizes $Q_l^m(z)$.

Lemma 2 We have

$$Q_l^m(z) = \frac{1}{2}P_l^{m+1}(z). \quad (22)$$

Proof See Section B. □

The following lemma characterizes $R_l^m(z)$.

Lemma 3 We have

$$R_l^m(z) = (l-m+1)(l+m)P_l^{m-1}(z). \quad (23)$$

Proof See Section B. □

Substituting Eq. (22) and Eq. (23) into Eq. (20, we have that when $m > 1$

$$Y_l^m(\theta+d\theta,\phi+d\phi)-Y_l^m(\theta,\phi) = c_z(-mY_l^{-m}(\theta,\phi)) + c_x\Big(\frac{K_l^m}{2K_l^{m+1}}Y_l^{-(m+1)}(\theta,\phi) + \frac{K_l^m(l-m+1)(l+m)}{K_l^{m-1}}Y_l^{-(m-1)}(\theta,\phi)\Big) + c_y\Big(-\frac{K_l^m}{2K_l^{m+1}}Y_l^{m+1}(\theta,\phi) + \frac{K_l^m(l-m+1)(l+m)}{K_l^{m-1}}Y_l^{m-1}(\theta,\phi)\Big)$$

When $m = 1$,

$$Y_l^1(\theta+d\theta,\phi+d\phi)-Y_l^1(\theta,\phi) = c_z(-Y_l^{-1}(\theta,\phi)) + c_x\Big(\frac{K_l^1}{2K_l^2}Y_l^{-2}(\theta,\phi) + \frac{K_l^1 l(l+1)}{\sqrt{2}K_l^0}Y_l^0(\theta,\phi)\Big) + c_y\Big(-\frac{K_l^1}{2K_l^2}Y_l^2(\theta,\phi) + \frac{K_l^1 l(l+1)}{\sqrt{2}K_l^0}Y_l^0(\theta,\phi)\Big)$$

Proofs of Key Lemmas

Proof of Lemma 1

We first consider $Y_l^m(\theta+d\theta,\phi+d\phi)$ for $m > 0$. Applying Prop. 1, we have

$$\begin{aligned} Y_l^m(\theta+d\theta,\phi+d\phi)-Y_l^m(\theta,\phi) &= -\sqrt{2}K_l^m\Big(\sin(m\phi)P_l^m(\cos(\theta))md\phi + \cos(m\phi)\frac{\partial P_l^m(\cos(\theta))}{\partial z}\sin(\theta)d\theta\Big) \\ &= -\sqrt{2}K_l^m\Big(mc_z\sin(m\phi)P_l^m(\cos(\theta)) - m(c_x\cos(\phi)+c_y\sin(\phi))\sin(m\phi)\frac{\cos(\theta)}{\sin(\theta)}P_l^m(\cos(\theta)) \\ &\quad + (c_y\cos(\phi)-c_x\sin(\phi))\cos(m\phi)\sin(\theta)\frac{\partial P_l^m(\cos(\theta))}{\partial z}\Big). \end{aligned} \quad (24)$$

Note that

$$\cos(\phi)\sin(m\phi) = \frac{\sin((m+1)\phi)) + \sin((m-1)\phi)}{2}, \quad (25)$$

$$\sin(\phi)\sin(m\phi) = \frac{\cos((m-1)\phi) - \cos((m+1)\phi)}{2}, \quad (26)$$

$$\sin(\phi)\cos(m\phi) = \frac{\sin((m+1)\phi) - \sin((m-1)\phi)}{2}, \quad (27)$$

$$\cos(\phi)\cos(m\phi) = \frac{\cos((m-1)\phi) + \cos((m+1)\phi)}{2}. \quad (28)$$

Substituting Eq. (25)-(28) into Eq. (24), we have

$$\begin{aligned}Y_l^m(\theta+d\theta,\phi+d\phi)-Y_l^m(\theta,\phi)+mc_zY_l^{-m}(\theta,\phi)=&\frac{\sqrt{2}K_l^m}{2}\Big(c_y\cos((m+1)\phi)\big(-m\frac{\cos(\theta)}{\sin(\theta)}P_l^m(\cos(\theta))-\sin(\theta)\frac{\partial P_l^m(\cos(\theta))}{\partial z}\big)\\&+c_y\cos((m-1)\phi))\big(m\frac{\cos(\theta)}{\sin(\theta)}P_l^m(\cos(\theta))-\sin(\theta)\frac{\partial P_l^m(\cos(\theta))}{\partial z}\big)\\&+c_x\sin((m+1)\phi)\big(m\frac{\cos(\theta)}{\sin(\theta)}P_l^m(\cos(\theta))+\sin(\theta)\frac{\partial P_l^m(\cos(\theta))}{\partial z}\big)\\&+c_x\sin((m-1)\phi)\big(m\frac{\cos(\theta)}{\sin(\theta)}P_l^m(\cos(\theta))-\sin(\theta)\frac{\partial P_l^m(\cos(\theta))}{\partial z}\big)\Big)\end{aligned}$$

Note that

$$\frac{\cos(\theta)}{\sin(\theta)}P_l^m(\cos(\theta))=\frac{z}{\sqrt{1-z^2}}P_l^m(z)|_{z=\cos(\theta)},\qquad \sin(\theta)\frac{\partial P_l^m(\cos(\theta)}{\partial z}=\sqrt{1-z^2}\frac{\partial P_l^m(z)}{\partial z}|_{z=\cos(\theta)}.$$

We have

$$\begin{aligned}&Y_l^m(\theta+d\theta,\phi+d\phi)-Y_l^m(\theta,\phi)+mc_zY_l^{-m}(\theta,\phi)\\=&\frac{\sqrt{2}K_l^m}{2}\Big(-c_y\cos((m+1)\phi)Q_l^m(\cos(\theta))+c_y\cos((m-1)\phi)R_l^m(\cos(\theta))+c_x\sin((m+1)\phi)Q_l^m(\cos(\theta))\\&+c_x\sin((m-1)\phi)R_l^m(\cos(\theta))\Big).\end{aligned}$$

We then consider $Y_l^{-m}(\theta+d\theta,\phi+d\phi)$ for $m>0$. Applying Prop. 1, we have

$$\begin{aligned}Y_l^{-m}(\theta+d\theta,\phi+d\phi)-Y_l^{-m}(\theta,\phi)=&\sqrt{2}K_l^m\Big(\cos(m\phi)P_l^m(\cos(\theta))md\phi-\sin(m\phi)\frac{\partial P_l^m(\cos(\theta))}{\partial z}\sin(\theta)d\theta\Big)\\=&\sqrt{2}K_l^m\Big(mc_z\cos(m\phi)P_l^m(\cos(\theta))-m(c_x\cos(\phi)+c_y\sin(\phi))\cos(m\phi)\frac{\cos(\theta)}{\sin(\theta)}P_l^m(\cos(\theta))\\&-(c_y\cos(\phi)-c_x\sin(\phi))\sin(m\phi)\sin(\theta)\frac{\partial P_l^m(\cos(\theta))}{\partial z}\Big).\end{aligned}\tag{29}$$

Substituting Eq. (25)-(28) into Eq. (29), we have

$$\begin{aligned}Y_l^{-m}(\theta+d\theta,\phi+d\phi)-Y_l^{-m}(\theta,\phi)-mc_zY_l^m(\theta,\phi)=&\frac{\sqrt{2}K_l^m}{2}\Big(c_x\cos((m+1)\phi)\big(-m\frac{\cos(\theta)}{\sin(\theta)}P_l^m(\cos(\theta))-\sin(\theta)\frac{\partial P_l^m(\cos(\theta))}{\partial z}\big)\\&+c_x\cos((m-1)\phi))\big(-m\frac{\cos(\theta)}{\sin(\theta)}P_l^m(\cos(\theta))+\sin(\theta)\frac{\partial P_l^m(\cos(\theta))}{\partial z}\big)\\&+c_y\sin((m+1)\phi)\big(-m\frac{\cos(\theta)}{\sin(\theta)}P_l^m(\cos(\theta)-\sin(\theta)\frac{\partial P_l^m(\cos(\theta))}{\partial z}\big)\\&+c_y\sin((m-1)\phi)\big(m\frac{\cos(\theta)}{\sin(\theta)}P_l^m(\cos(\theta))-\sin(\theta)\frac{\partial P_l^m(\cos(\theta))}{\partial z}\big)\Big)\\=&\sqrt{2}K_l^mc_x\big(-\cos((m+1)\phi)Q_l^m(\cos(\theta))-\cos((m-1)\phi)R_l^m(\cos(\theta))\big)\\&+\sqrt{2}K_l^mc_y\big(-\sin((m+1)\phi)Q_l^m(\cos(\theta))+\sin((m-1)\phi)R_l^m(\cos(\theta))\big),\end{aligned}$$

Proof of Lemma 2

Proof First, we have

$$\frac{mz}{\sqrt{1-z^2}}P_l^m=\frac{(-1)^l}{2^ll!}mz(1-z^2)^{\frac{m-1}{2}}\frac{\partial^{l+m}(z^2-1)^l}{\partial^{l+m}z}.\tag{30}$$

Moreover,

$$\begin{aligned}\sqrt{1-z^2}\frac{\partial P_l^m(z)}{\partial z}=&\sqrt{1-z^2}\frac{(-1)^l}{2^ll!}\frac{\partial}{\partial z}\Big((1-z^2)^{\frac{m}{2}}\frac{\partial^{l+m}(z^2-1)^l}{\partial^{l+m}z}\Big)\\=&-\frac{(-1)^l}{2^ll!}mz(1-z^2)^{\frac{m-1}{2}}(1-z^2)^{\frac{m-1}{2}}\frac{\partial^{l+m}(z^2-1)^l}{\partial^{l+m}z}+\frac{(-1)^l}{2^ll!}(1-z^2)^{\frac{m+1}{2}}\frac{\partial^{l+m+1}(z^2-1)^l}{\partial^{l+m+1}z}.\end{aligned}\tag{31}$$

Combing Eq. (30) and Eq. (31), we have

$$Q_l^m(z) = \frac{1}{2}\frac{(-1)^l}{2^l l!}(1-z^2)^{\frac{m+1}{2}}\frac{\partial^{l+m+1}(z^2-1)^l}{\partial^{l+m+1}z} = \frac{1}{2}P_l^{m+1}(z).$$

□

Proof of Lemma 3

Again combing Eq. (30) and Eq. (31), we have

$$R_l^m(z) = \frac{1}{2}\frac{(-1)^l}{2^l l!}(1-z^2)^{\frac{m-1}{2}}\left(2mz\frac{\partial^{l+m}(z^2-1)^l}{\partial^{l+m}z} + (z^2-1)\frac{\partial^{l+m+1}(z^2-1)^l}{\partial^{l+m+1}z}\right) \tag{32}$$

As $(z^2-1)^l = \sum_{k=0}^{l}\frac{(-1)^k l!}{k!(l-k)!}z^{2l-2k}$, it follows that

$$\frac{\partial^{l+m}(z^2-1)^l}{\partial^{l+m}z} = \sum_{k=0}^{\lfloor\frac{l-m}{2}\rfloor}(-1)^k\frac{l!(2l-2k)!}{k!(l-k)!(l-2k-m)!}z^{l-2k-m}, \tag{33}$$

$$\frac{\partial^{l+m+1}(z^2-1)^l}{\partial^{l+m+1}z} = \sum_{k=0}^{\lfloor\frac{l-m}{2}\rfloor}(-1)^k\frac{l!(2l-2k)!}{k!(l-k)!(l-2k-m-1)!}z^{l-2k-m-1}. \tag{34}$$

Substituting (33) and (34) into (32), we have

$$R_l^m(z) = \frac{1}{2}\frac{(-1)^l}{2^l l!}(1-z^2)^{\frac{m-1}{2}}\sum_{k=0}^{\lfloor\frac{l-m}{2}\rfloor}(-1)^k z^{l-2k-m+1}\frac{l!(2l-2k)!}{k!(l-k)!(l-2k-m)!}\Big(l-2k+m + \frac{2k(2l-2k+1)}{(l-2k-m+1)}\Big) \tag{35}$$

Moreover,

$$P_l^{m-1}(z) = \frac{(-1)^l}{l!2^l}(1-z^2)^{\frac{m-1}{2}}\sum_{k=0}^{\lfloor\frac{l-m+1}{2}\rfloor}\frac{(-1)^k l!}{k!(l-k)!}\frac{(2l-2k)!}{(l-2k-m+1)!}$$

Note that

$$\begin{aligned}&(l-2k-m+1)(l-2k+m)+2k(2l-2k+1)\\ =&(l-m+1)(l+m)+4k^2-4k^2-2k(2l-1)+2k(2l-1) = (l-m+1)(l+m).\end{aligned}$$

This means $R_l^m(z) = (l-m+1)(l+m)P_l^{m-1}(z)$. which ends the proof.

Appendix C: Proof of Propositions in Section 6

Proof of Prop 2

Suppose $f(\theta+\frac{2i\pi}{k}) = f(\theta),\ \forall\theta\in[0,\frac{2\pi}{k})$. We have

$$\begin{aligned}c_{2i-1}^f &= \int_0^{2\pi} f(\theta)\sin(i\theta)d\theta\\ &= \sum_{j=0}^{k-1}\int_0^{\frac{2\pi}{k}} f(\theta)\sin(i\theta+\frac{2ij\pi}{k})d\theta\\ &= \int_0^{2\pi} f(\theta)\Big(\frac{1}{k}\sum_{j=0}^{k-1}\sin(\frac{i\theta+2ij\pi}{k})\Big)d\theta\\ &= \int_0^{2\pi} f(\theta)\big(\sin(\frac{i\theta}{k})a_{ijk}+\cos(\frac{i\theta}{k})b_{ijk}\big)d\theta\end{aligned}$$

where

$$a_{ijk} = \frac{1}{k}\sum_{j=0}^{k-1}\cos(\frac{2ij\pi}{k}),\quad b_{ijk} = \frac{1}{k}\sum_{j=0}^{k-1}\sin(\frac{2ij\pi}{k}).$$

Note that

$$\begin{aligned} a_{ijk}\sin(\frac{i\pi}{k}) &= \frac{1}{k}\sum_{j=0}^{k-1}\cos(\frac{2ij\pi}{k})\sin(\frac{i\pi}{k}) \\ &= \frac{1}{2k}\sum_{j=0}^{k-1}\big(\sin(\frac{(2j+1)i\pi}{k}) - \sin(\frac{(2j-1)i\pi}{k})\big) \\ &= \frac{1}{2k}\Big(\sin(\frac{(2k-1)i\pi}{k}) - \sin(\frac{-i\pi}{k})\Big) = 0. \end{aligned}$$

When $\mathrm{mod}(i,k) \neq 0$, $\sin(\frac{i\pi}{k}) \neq 0$. This means $a_{ijk} = 0$. If $\mathrm{mod}(i,k) = 0$, then $a_{ijk} = 1$. Through similar calculations, when $\mathrm{mod}(i,k) \neq 0$, $b_{ijk} = 0$. If $\mathrm{mod}(i,k) = 0$, then $b_{ijk} = 0$.

Appendix D: Patterns of l: Zero Spherical Harmonic Coefficients

Let G be a finite subgroup of $\mathrm{SO}(3)$. A spherical harmonic Y_l^m is invariant under G if $\forall g \in G$, $Y_l^m(g\cdot\mathbf{x}) = Y_l^m(\mathbf{x})$. This means that Y_l^m lies in the trivial representation of G within the degree-l representation. Consider the invariant projection operator for group G

$$P_G f(\mathbf{x}) = \frac{1}{|G|}\sum_{g\in G} f(g\cdot\mathbf{x}) \tag{36}$$

which projects any function f onto the subspace of functions invariant under G. Let $V_l = \mathrm{Span}\{Y_l^m : -l \leqslant m \leqslant l\}$ be the $(2l+1)$-dimensional irreducible representation of $\mathrm{SO}(3)$. The invariant projection operator of G at degree l is

$$P_{G|V_l} = \frac{1}{|G|}\sum_{g\in G} D^l(g) \tag{37}$$

where $D^l(g)$ is the Wigner-D matrix. If $\mathrm{rank}(P_{G|V_l}) > 0$, then there is at least one linear combination of Y_l^m that is invariant under all $g \in G$. Otherwise, all spherical harmonic coefficients at degree l must be zero and thus $f_l = 0$.

An easy way to compute the rank is by taking the matrix trace, or in other words, computing the character function of the representations. This also gives the multiplicity m_l^G of the trivial representation in V_l

$$m_l^G = \frac{1}{|G|}\sum_{g\in G}\chi_l(g), \tag{38}$$

where $|G|$ is the order of the group, χ_l is the character function of the degree-l representation of $\mathrm{SO}(3)$. For any 3D rotation $g \in \mathrm{SO}(3)$, the character $\chi_l(g)$ only depends on its rotation angle θ,

$$\chi_l(g) = \frac{\sin((2l+1)\theta/2)}{\sin(\theta/2)}. \tag{39}$$

The character functions are constant on each conjugation class, and 3D rotations with the same angle are from the same conjugation class. Therefore, we can also calculate the trivial-representation multiplicity in V_l with

$$m_l^G = \frac{1}{|G|}\sum_k n_k\,\chi_l(\theta_k), \tag{40}$$

where n_k is the number of elements in the k-th conjugation class and θ_k is the corresponding rotation angle.

Cyclic group C_n The rotations in the cyclic group C_n are of angles $\theta_k = 2\pi k/n,\ k = 0,\cdots,n-1$. The trivial-representation multiplicity is

$$m_l^{C_n} = \frac{1}{n}\sum_{k=0}^{n-1}\chi_l\left(\frac{2\pi k}{n}\right) = \frac{1}{n}\sum_{k=0}^{n-1}\sum_{m=-l}^{l} e^{-im\frac{2\pi k}{n}} = \frac{1}{n}\sum_{m=-l}^{l}\sum_{k=0}^{n-1} e^{-im\frac{2\pi k}{n}}. \tag{41}$$

Observe that

$$\sum_{k=0}^{n-1} e^{-im\frac{2\pi k}{n}} = \begin{cases} n & \text{if } m \equiv 0 \mod n \\ 0 & \text{otherwise} \end{cases}. \tag{42}$$

Thus, $m_l^{C_n} = \#\{m \in [-l,l] : m \equiv 0 \mod n\} = \lfloor 2l/n \rfloor + 1$. There is no l that makes $m_l^{C_n}$ vanish.

Dihedral group D_n The Dihedral group D_n contains all rotations in the cyclic group C_n, plus n reflections through the axes perpendicular to the main one. The trivial-representation multiplicity is

$$m_l^{D_n} = \frac{1}{2n}\left(\sum_{k=0}^{n-1}\chi_l\left(\frac{2\pi k}{n}\right)+\sum_{k=0}^{n-1}\chi_l(\pi)\right) = \frac{1}{2}\left(\left\lfloor\frac{2l}{n}\right\rfloor+1+(-1)^l\right). \tag{43}$$

For any $n>2$, odd l makes $m_l^{D_n}=0$.

Tetrahedral group T The conjugation classes are

Rotation angle	0	$2\pi/3$	π
#Elements	1	8	3

The trivial-representation multiplicity is

$$m_l^T = \frac{1}{12}(\chi_l(0)+8\chi_l(2\pi/3)+3\chi_l(\pi)) = \frac{1}{12}\left((2l+1)+8\frac{\sin((2l+1)\pi/3)}{\sin(\pi/3)}+3(-1)^l\right), \tag{44}$$

giving the non-zero coefficients $f_l = 0,3,4,6,7,9,10,\cdots$.

Octahedral group O The conjugation classes are

Rotation angle	0	π	$2\pi/3$	$\pi/2$
#Elements	1	6	8	9

The trivial-representation multiplicity is

$$m_l^O = \frac{1}{24}(\chi_l(0)+6\chi_l(\pi)+8\chi_l(2\pi/3)+9\chi_l(\pi/2)), \tag{45}$$

giving the non-zero coefficients $f_l = 0,4,6,8,9,10,12,\cdots$.

Icosahedral I The conjugation classes are

Rotation angle	0	$2\pi/5$	$4\pi/5$	$2\pi/3$	π
#Elements	1	15	15	20	24

The trivial-representation multiplicity is

$$m_l^I = \frac{1}{60}(\chi_l(0)+15\chi_l(2\pi/5)+15\chi_l(4\pi/5)+20\chi_l(2\pi/3)+24\chi_l(\pi)), \tag{46}$$

giving the non-zero coefficients $f_l = 0,6,10,12,15,16,18,20,\cdots$.

Appendix E: Analysis of Weighted L^2 Norm

We provide an argument on the importance of using non-uniform weights in the presence of vanishing SH coefficients. Although the objective function employed in relative rotation estimation is non-linear, the local refinement operates in a local regime, in which we can approximate a rotation using a linear map. In light of this view, we opt to study a simple linear least-square problem, whose behavior offers justification of using non-uniform weights. Specifically, consider the fitting problem of optimizing x to minimize the following weighted minimization problem:

$$\min_x w_1(a_1x-b_1)^2+w_2(a_2x-b_2)^2. \tag{47}$$

The first term corresponds to constraints provided by non-vanishing coefficients; a_1 and b_1 are independent and they satisfy

$$a_1 \sim \mathcal{U}[f-\epsilon, f+\epsilon], \qquad b_1 \sim \mathcal{U}[fc-\epsilon, fc+\epsilon].$$

The second term corresponds the constraints provided by vanishing coefficients; a_2 and b_2 are independent and they satisfy

$$a_2 \sim \mathcal{U}[-\epsilon,\epsilon], \qquad b_2 \sim \mathcal{U}[-\epsilon,\epsilon].$$

It is clear that the optimal x in (47) is given by

$$x^\star = \frac{w_1a_1b_1+w_2a_2b_2}{w_1a_1^2+w_2a_2^2}.$$

The designed value of $x^\star$ is c. As $x^\star$ only depends on the ratio between w_1 and w_2, we fix $w_1 = 1$ and define a function $s(w_2)$ as

$$\begin{aligned} s(w_2) &= \mathbb{E}_{a_1,a_2,b_1,b_2}(x^\star - c)^2 \qquad (48)\\ &= \mathbb{E}_{a_1,a_2,b_1,b_2}\Big(\big(\frac{a_1b_1 + w_2a_2b_2}{a_1^2 + w_2a_2^2}\big)^2 - 2c\big(\frac{a_1b_1 + w_2a_2b_2}{a_1^2 + w_2a_2^2}\big) + c^2\Big)\\ &= \mathbb{E}_{a_1,a_2}\Big(\frac{a_1^2(f^2c^2 + \frac{2\epsilon^2}{3}) + w_2^2a_2^2\frac{2\epsilon^2}{3}}{\big(a_1^2 + w_2a_2^2\big)^2} - 2c\frac{a_1fc}{a_1^2 + w_2a_2^2} + c^2\Big)\\ &= \mathbb{E}_{a_1,a_2}\frac{c^2\big(a_1(a_1 - f) + w_2a_2^2\big)^2 + (a_1^2 + w_2^2a_2^2)\frac{2\epsilon^2}{3}}{\big(a_1^2 + w_2a_2^2\big)^2}. \qquad (49) \end{aligned}$$

We show that when $c \neq 0$

$$s(0) < s(1). \qquad (50)$$

In fact,

$$\begin{aligned} s(0) &= \frac{2\epsilon^2}{3}\mathbb{E}_{a_1}\frac{1}{a_1^2} + c^2\mathbb{E}_{a_1}\frac{(a_1 - f)^2}{a_1^2}\\ &= \sum_{i=1}^{\infty}\big(\frac{2}{3} + \frac{2ic^2}{(2i+1)}\big)\frac{\epsilon^{2i}}{f^{2i}}. \end{aligned}$$

Moreover,

$$s(1) = c^2 + \mathbb{E}_{a_1,a_2}\frac{\frac{2\epsilon^2}{3} - 2c^2a_1f}{a_1^2 + a_2^2} + \mathbb{E}_{a_1,a_2}\frac{c^2f^2a_1^2}{(a_1^2 + a_2^2)^2}. \qquad (51)$$

Note that,

$$\begin{aligned} \mathbb{E}_{a_1,a_2}\frac{1}{a_1^2 + a_2^2} &= \sum_{i=0}^{\infty}\mathbb{E}_{a_1}a_1^{-2-2i}(-1)^i\mathbb{E}_{a_2}a_2^{2i}\\ &= \sum_{i=0}^{\infty}\frac{1}{2i+1}\mathbb{E}_{a_1}a_1^{-2-2i}(-1)^i\epsilon^{2i}\\ &= \sum_{i=0}^{\infty}\frac{1}{2\epsilon(2i+1)^2}\Big((f-\epsilon)^{-(2i+1)} - (f+\epsilon)^{-(2i+1)}\Big)(-1)^i\epsilon^{2i} \qquad (52) \end{aligned}$$

Moreover,

$$\begin{aligned} \mathbb{E}_{a_1,a_2}\frac{a_1}{a_1^2 + a_2^2} &= \sum_{i=0}^{\infty}\mathbb{E}_{a_1}a_1^{-1-2i}(-1)^i\mathbb{E}_{a_2}a_2^{2i}\\ &= \sum_{i=0}^{\infty}\frac{1}{2i+1}\mathbb{E}_{a_1}a_1^{-1-2i}(-1)^i\epsilon^{2i}\\ &= \frac{1}{f}\sum_{i=}^{\infty}\frac{\epsilon^{2i}}{f^{2i}} + \sum_{i=1}^{\infty}\frac{1}{2\epsilon(2i+1)(2i)}\Big((f-\epsilon)^{-2i} - (f+\epsilon)^{-2i}\Big)(-1)^i\epsilon^{2i} \qquad (53) \end{aligned}$$

Furthermore,

$$\begin{aligned} \mathbb{E}_{a_1,a_2}\frac{a_1^2}{(a_1^2 + a_2^2)^2} &= \sum_{i=0}^{\infty}\mathbb{E}_{a_1}a_1^{-2-2i}(-1)^i(2i+1)\mathbb{E}_{a_2}a_2^{2i}\\ &= \sum_{i=0}^{\infty}\mathbb{E}_{a_1}a_1^{-2-2i}(-1)^i\epsilon^{2i}\\ &= \sum_{i=0}^{\infty}\frac{1}{2\epsilon(2i+1)}\Big((f-\epsilon)^{-(2i+1)} - (f+\epsilon)^{-(2i+1)}\Big)(-1)^i\epsilon^{2i} \qquad (54) \end{aligned}$$

Substituting Eqs. (52), (53), and (54) into (51), we have

$$s(1) \approx \frac{2}{3} + \frac{4c^2}{3}\frac{\epsilon^2}{f^2}.$$

This means $s(0) < s(1)$ when $c \neq 0$, which ends the analysis.

Appendix F: Local Convergence Analysis

We provide a local convergence analysis of the optimization strategy in a more general setting. Suppose that we have n pairs of vectors $f_i(x)$ and g_i, where x is the optimization variable. As the norm of the spherical harmonics coefficient vector is fixed under rotation, we can model the objective function as

$$f(x) = \sum_{i=1}^{N} w_i(x)\|f_i(x) - g_i\|^2, \qquad w_i(x) = \exp\Big(-\frac{\|f_i(x)-g_i\|^2}{2\sigma_i^2}\Big). \tag{55}$$

We study the convergence of our alternate minimization strategy in the vicinity of a local minimum $x^\star$. Introduce

$$H(x) = \sum_{i=1}^{n} w_i(x)\frac{\partial f_i}{\partial x}(x)^T\frac{\partial f_i}{\partial x}(x) \tag{56}$$

$$F(x) = \sum_{i=1}^{n} w_i(x)\Big(\frac{\frac{\partial f_i(x^\star)}{\partial x}^T\big(f_i(x)-g_i\big)}{\sigma_i}\Big)\Big(\frac{\frac{\partial f_i(x)}{\partial x}^T\big(f_i(x)-g_i\big)}{\sigma_i}\Big)^T \tag{57}$$

$$G(x) = \sum_{i=1}^{n} w_i(x)\frac{\partial^2 f_i}{\partial^2 x}(x)^T(g_i - f_i(x)) \tag{58}$$

Theorem 3 If $H(x^\star)$, $F(x^\star)$, and $G(x^\star)$ satisfy

$$\|H(x^\star)^{-1}F(x^\star)\| + \|H(x^\star)^{-1}G(x^\star)\| < 1, \tag{59}$$

then there exists a radius δ, so that starting from x_0 where $\|x_0 - x^\star\| \le \delta$, the alternating minimization procedure converges to $x^\star$ with a linear convergence rate.

Proof Denote the value of x at the k-th iteration as x_{k+1}. Then

$$\begin{aligned} x_{k+1} &= \operatorname*{argmin}_x \sum_{i=1}^{n} w_i(x_k)\|f_i(x_k) + \frac{\partial f_i}{\partial x}(x_k)(x-x_k) - g_i\|^2 \\ &= x_k + H(x_k)^{-1}g(x_k) \end{aligned} \tag{60}$$

where

$$g(x) = \sum_{i=1}^{n} w_i(x)\frac{\partial f_i}{\partial x}(x)^T\big(g_i - f_i(x)\big).$$

Applying Taylor expansion, we have

$$w_i(x_k) = w_i(x^\star)\Big(1 - \Big(\frac{\frac{\partial f_i(x^\star)}{\partial x}^T\big(f_i(x^\star)-g_i\big)}{\sigma_i^2}\Big)^T(x_k - x^\star)\Big) + O(\|x_k - x^\star\|^2).$$

It follows that

$$\begin{aligned} g(x_k) =& -\sum_{i=1}^{n} w_i^\star\Big(\frac{\frac{\partial f_i(x^\star)}{\partial x}^T\big(f_i(x^\star)-g_i\big)}{\sigma_i}\Big)\Big(\frac{\frac{\partial f_i(x^\star)}{\partial x}^T\big(f_i(x^\star)-g_i\big)}{\sigma_i}\Big)^T(x_k - x^\star) \\ &+ \sum_{i=1}^{n} w_i^\star\frac{\partial^2 f_i}{\partial^2 x}(x_k)^T\big(g_i - f_i(x^\star)\big)(x_k - x^\star) - H(x^\star)(x_k - x^\star) + O(\|x_k - x^\star\|^2) \qquad (61) \\ =& \big(-F(x^\star) + G(x^\star) - H(x^\star)\big)(x_k - x^\star) + O(\|x_k - x^\star\|^2). \qquad (62) \end{aligned}$$

Therefore,

$$x_{k+1} - x^\star = H(x^\star)^{-1}\big(-F(x^\star) + G(x^\star)\big)(x_k - x^\star) + O(\|x_k - x^\star\|^2).$$

This means if Eq. (59) is satisfied, $\|x_{k+1} - x^\star\| \le c\|x_k - x^\star\|$ for $c < 1$ and in a small neighborhood of $x^\star$. This ends the proof. □